Study of a low Mach nuclear core model for two-phase flows with phase transition II: tabulated equation of state

Stéphane Dellacherie, Gloria Faccanoni, Bérénice Grec, Yohan Penel

Study of a low Mach nuclear core model for two-phase flows with phase transition II: Tabulated equation of state

Stéphane Dellacherie[*], Gloria Faccanoni[‡], Bérénice Grec[§], Yohan Penel[¶]

January 8, 2016

In order to model the water flow in a nuclear reactor core, the authors carried out several studies coupling the Low Mach nuclear core (Lmnc) model of partial differential equations to the stiffened gas law for the physical behaviour. The Lmnc model is derived from the Navier-Stokes equations through an asymptotic expansion with respect to the Mach number commonly assumed to be small in this domain of application. This simplified system of equations provides qualitative results under the stiffened gas hypothesis such as analytical solutions in dimension 1 and enables a simple numerical treatment no matter what the dimension.

In the regime of interest (namely high pressure situations), the stiffened gas law turns out to be inaccurate. That is why this paper is devoted to the coupling of the Lmnc model to an equation of state tuned by means of experimental values (NIST) for thermodynamic variables. The very point in this study consists in fitting tabulated values and derivatives satisfying positivity and monotonicity constraints, showing a clear improvement in the quantitive results.

1 Introduction

The modelling of fluid flows requires two closely related elements: a system of partial differential equations (PDEs) governing the overall behaviour of the fluid (involving velocity, temperature and pressure for example) and an equation of state (EOS) that characterises some properties of the fluid (*e.g.* density, viscosity, ...). More precisely, an EOS may be an algebraic or a differential relation between thermodynamic variables (temperature, pressure, entropy, internal energy and specific volume) which enables to express them as a function of only two variables. The coefficients involved in the EOS are tuned depending on the fluid and on the experiment.

A model in fluid mechanics is thus the combination of a system of PDEs and an EOS. Without any of them, the model would be ill-posed (from a mathematical point of view) and inconsistent (from a physical point of view). As far as the PDEs are concerned, there exists a wide family of systems mainly resulting from the Navier-Stokes equations (supplemented with source terms depending on the underlying physical phenomenon) under simplifying assumptions. These equations primarily belong to the hyperbolic kind (or parabolic if viscosity effects are involved). But for the EOS, there is no ultimate formula which is altogether consistent with all thermodynamic constraints (derivation from an entropy, positivity of the squared speed of sound, ...) and relevant for a wide range of applications.

On the one hand, the ideal gas law is so simple that applications are restricted to gas in standard conditions. On the other hand, cubic equations like the Van der Waals law have a wider domain of validity but their more complex expressions prevent from achieving analytical results and lead to an imaginary speed of sound (loss of hyperbolicity when coupled to the Euler system) within the saturation dome where both liquid and vapour co-exist (see liquid-vapour mixture on Fig. 2a). This shows that it is intricate to find a balance between mathematical and physical requirements, in particular when phase transition occurs.

[*]DEN/DANS/DM2S/STMF, Commissariat à l'Énergie Atomique et aux Énergies Alternatives – Saclay, 91191 Gif-sur-Yvette, France – stephane.dellacherie@cea.fr

[†]Département de Génie Mécanique, École Polytechnique de Montréal, C.P. 6079, succ. Centre-ville, Montréal (Québec), H3C 3A7, Canada

[‡]Université de Toulon – IMATH, EA 2134, avenue de l'Université, 83957 La Garde, France – faccanon@univ-tln.fr

[§]MAP5 UMR CNRS 8145 - Université Paris Descartes - Sorbonne Paris Cité, 45 rue des Saints Pères, 75270 Paris Cedex 6, France – berenice.grec@parisdescartes.fr

[¶]CEREMA–Inria (team ANGE) and Sorbonne Universités, UPMC Univ. Paris 06, LJLL UMR CNRS 7598, 75005 Paris, France – yohan.penel@cerema.fr

A commonly used EOS to describe a pure phase is the stiffened gas (SG) law, presented in [15] and derived in [20, Ch. VII] as a linearisation of the Grüneisen EOS under the hypothesis of small density variations. To adapt to different materials and different physical situations, the SG law comprises 5 parameters which are tuned in order to match experimental data [18]. No matter what useful, the SG law turns out to become irrelevant for high temperatures (beyond 500 K for water) and high pressures (around 155 bar) which is mainly the case in the applications we are interested in, namely the modelling of the coolant in a nuclear reactor. This is due to the fact that the SG law relies on a linear relation between enthalpy and temperature, which is no more valid close to the critical point.

Judging from the fact that no analytical EOS seems to be able to model the behaviour of a pure phase at any temperature and pressure, one may use tabulated experimental values. The NIST library [19], which is widely used, contains tabulated values of many variables for many elements. These tables enable to provide relevant values by means of fitting processes no matter what the regime of the fluid. The reader may refer to [12,17] where compressible fluids are simulated with phase transition. One should however pay attention to potential problems of accuracy when approximating derivatives as many variables are recovered through differential formulae (see [10] for instance).

In previous papers, the authors investigated the modelling of the coolant in a nuclear reactor core. The study is based on the fact that time scales (material, acoustic) are dramatically different due to the weak compressibility of the water. Indeed, the Mach number is typically small in this framework. As a result, models can be simplified through the low Mach assumption which in particular decouples the thermodynamic pressure (involved in the EOS) from the dynamic pressure (appearing in the momentum conservation law). This procedure – an asymptotic expansion with respect to the Mach number – results in equations easier to analyse and to simulate numerically. Although acoustic waves have been filtered out, the model allows for large heat transfers unlike incompressible models.

The low Mach approach is complementary to studies carried out with thermodynamic industrial codes and based on compressible models. On the one hand, this approach provides theoretical and numerical information to better understand thermohydraulic processes at low Mach numbers. On the other hand, it can be used to assess compressible codes as compressible numerical schemes suffer a lack of accuracy in the low Mach regime.

The LMNC model[1] was first derived in [8]. It includes fission reaction terms, thermal conductivity, viscosity effects and time-varying boundary conditions. Coupled to the SG law, 1D steady solutions can be derived when thermal conductivity is ignored [8]. 1D unsteady solutions were presented in [2] for a monophasic fluid and then in [3] with phase transition. These preliminary results were extended to dimension 2 in [9].

However, temperatures at stake in a nuclear reactor core may become higher than the domain of validity of the SG law. That is why we focus in this paper on tabulated values extracted from the NIST library. We can observe on Figure 1 the growing discrepancy between values computed from the SG law and from measurements. The overestimation of the temperature at saturation due to the SG EOS could lead to unreliable results especially in the framework of safety evaluations of nuclear power plants. We mention that our treatment is specific to the collection of variables used in the LMNC model considering water in a pressurised water reactor (PWR), but it may be easily adapted to other pressure values and/or species.

The paper is structured as follows. We recall in Section 2 the basis of thermodynamics and present the way we model the mixture phase and how we use tabulated values to compute equations of state in pure liquid and vapour phases. It includes comparisons of graphs of SG and tabulated EOS in the relevant range of enthalpy values. Section 3 is dedicated to the setting of the differential model (LMNC) including boundary conditions and physical or mathematical assumptions. We also introduce thermal conduction processes in the modelling. We then focus in Section 4 on the incorporation of this new kind of equation of state in existing 1D and 2D schemes adapted to thermal diffusion. These schemes are applied to different configurations in Section 5 where the influence of thermal diffusion and gravity orientation is discussed.

2 Thermodynamics of a two-phase fluid

The thermodynamic properties of a fluid are modelled by an equation of state (EOS) which consists of an algebraic/differential relation between thermodynamic variables. The issue is to derive an EOS that models pure liquid and vapour phases of a fluid as well as the transition from one phase to another in a relevant and accurate way since perturbations of data may dramatically modify the temperature at saturation in the fluid and cause unphysical phase transition from liquid phase to vapour phase.

In the present study, water can appear under liquid or vapour phase or as a mixture of both phases as we consider the fluid a continuum (see [23, 26] for a review of multiphase flow modelling). The overall problem could be treated by means of distinct models for each phase supplemented with transmission conditions where phase transition occurs as it is the case for immiscible fluids.

Our model relies on the assumption of local kinematic and thermodynamical equilibria between phases. This means that phases are assumed to evolve at the same velocity, and that vaporisation, condensation and heat transfer processes are assumed to be instantaneous. As a result, we model the two-phase flow by means of a single system of

---

[1]LMNC stands for *Low Mach Nuclear Core*.

PDEs governing physical variables no matter what phase they are related to. This process only holds provided the EOS has a wide domain of validity including phase transition. For more details on the construction of these EOS and their applications to CFD for compressible fluid flows, see for instance [1, 6, 11, 13, 17, 25].

2.1 General thermodynamics

In classical thermodynamics two variables are sufficient to represent a thermodynamic state for a pure single-phase fluid (the corresponding relation is called an EOS). In the literature there exist numerous EOS specific to the fluid which is considered. In the case of liquid-vapour phase transitions, the EOS must not only represent the behaviour of each pure phase (liquid or vapour), but also model the evolution of the mixture. Its behaviour is schematically depicted on Figure 2 and represented by means of experimental data extracted from [19] on Figure 3.

When phase transition is taken into account, a mixture zone appears where the two phases coexist: it is called the *saturation zone* (Figs. 2a and 3a). This region is bounded by two saturation curves connected at the critical point $(1/\rho_c, p_c)$ which also belongs to the critical isotherm $T = T_c$. Since phase transition appears at constant pressure and temperature, the physical isotherm is horizontal in the mixture region and coincide with the isobar. At the critical point C, the isotherm $T = T_c$ has a horizontal tangent.

Another curve of interest is the coexistence curve $T \mapsto p^s(T)$ which relates the pressure to the temperature at saturation (see Figs. 2b and 3b).

Nevertheless, it is very complicated to derive a unique EOS describing accurately both pure and mixture phases. To better handle each phase, an idea consists in using two laws (one for each phase) so that each phase has its own thermodynamics. In the following sections we detail the general construction of the EOS: firstly (section 2.2) in the mixture region given saturated values for each phase (which is a standard procedure, see [5]) and secondly (section 2.3) in pure phases based on tabulated values.

We consider each phase κ ($\kappa = \ell$ for the liquid phase and $\kappa = g$ for the vapour phase) a compressible fluid governed by a given EOS that is, following [5], a function $(\rho, \varepsilon) \mapsto \mathcal{S}_\kappa(\rho, \varepsilon)$ where ρ, ε and $\mathcal{S}_\kappa$ denote respectively the specific density, the specific internal energy and the specific entropy of the fluid. We assume that $\partial_\varepsilon \mathcal{S}_\kappa > 0$ and $\mathcal{S}_\kappa$ has a *negative-definite Hessian matrix* [5].

We then define classically for phase $\kappa \in \{\ell, g\}$

- the temperature $T_\kappa(\rho, \varepsilon) \stackrel{\text{def}}{=} 1/\left[(\partial \mathcal{S}_\kappa/\partial \varepsilon)_\rho\right]$,

- the pressure $p_\kappa(\rho, \varepsilon) \stackrel{\text{def}}{=} -\rho^2 T_\kappa (\partial \mathcal{S}_\kappa/\partial \rho)_\varepsilon$,

- the Gibbs potential $G_\kappa(\rho, \varepsilon) \stackrel{\text{def}}{=} \varepsilon + p_\kappa/\rho - T_\kappa \mathcal{S}_\kappa$.

The choice of variables (ρ, ε) is in particular motivated by the fact that inside the mixture zone, ρ and $\rho\varepsilon$ depend linearly on the volume fraction – see (1) below. Classical thermodynamic differential equations enable to express thermodynamic potentials $(\varepsilon, h, G, \dots)$ as a function of their associated natural variables, like the Gibbs potential $G(p, T)$. Due to the smoothness hypotheses upon $\mathcal{S}$, we can switch into any combination of variables, such as (p, T) (to characterise the saturation data) or (h, p) (which is well suited to the system of equations we consider).

2.2 Construction of the EOS in the mixture

In the following paragraphs, we recall the expressions in the mixture for the density, the temperature, the compressibility coefficient, the viscosity, the heat conductivity and the speed of sound of two-phase media no matter what the EOS modelling the pure phases. The mixture EOS only depends on values at saturation. Thus, the construction is the same as the one presented in [3]. The novelty is the computation of the EOS for each pure phase by means of tables and it will be detailed in Section 2.3.

Characterisation of the two-phase media   When taking phase transition into account, the two-phase mixture is constructed according to the second principle of thermodynamics. The key idea is that, when phases coexist in a same unit volume, they have the same temperature, the same pressure and their chemical potentials are equal. The corresponding temperature, noted T^s for *temperature at saturation*, is obtained by expliciting the equality of Gibbs potentials $G_\ell(p, T^s) = G_g(p, T^s)$. This implies a relation between T^s and p (see for example [5, 11, 14] for more details). In the sequel we choose to express the temperature in the mixture as a function of the pressure and we define functions at saturation ρ_κ^s and h_κ^s by $p \mapsto \rho_\kappa^s \stackrel{\text{def}}{=} \rho_\kappa\big(p, T^s(p)\big)$ and $p \mapsto h_\kappa^s \stackrel{\text{def}}{=} h_\kappa\big(p, T^s(p)\big)$. The choice to focus on pressure relies on the fact that the pressure in the LMNC model is supposed to be constant and equal to p_0 (see Section 3.1).

What follows heavily relies on the assumption $h_\ell^s(p) < h_g^s(p)$, which is the case for most fluids (see [19] and [3, Rem. 2.1]). Moreover, we shall usually note h_κ^s rather than $h_\kappa^s(p)$.
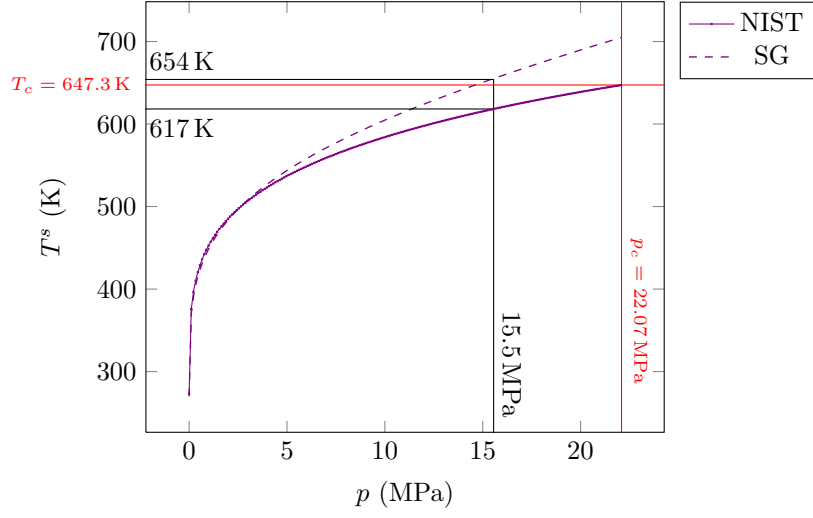
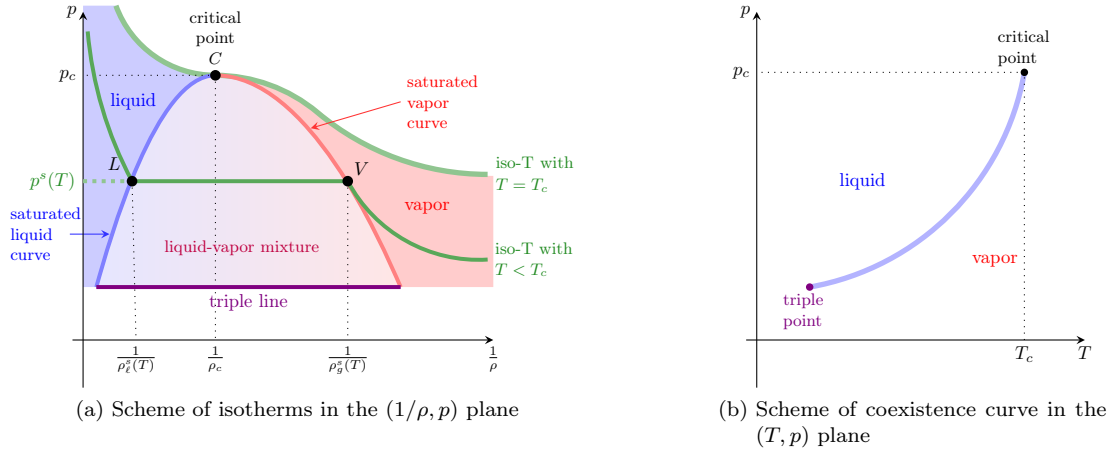Figure 1: Temperature at saturation as a function of the pressure

(a) Scheme of isotherms in the $(1/\rho, p)$ plane

(b) Scheme of coexistence curve in the (T, p) plane

Figure 2: Schematic saturation and coexistence curves.

(a) Isotherms in the $(1/\rho, p)$ plane (b) Coexistence curve in the (T, p) plane
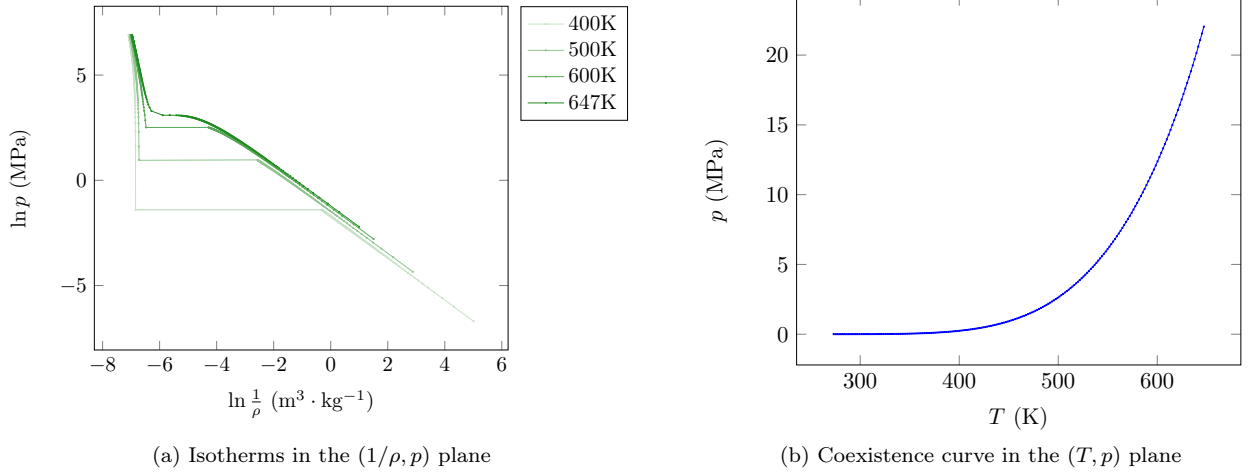
Figure 3: Saturation and coexistence curves using experimental data from [19]

Let α be the volume fraction of vapour phase. This variable characterizes the volume of vapour in each unit volume: $\alpha = 1$ means that this volume is completely filled by vapour whereas a full liquid volume corresponds to $\alpha = 0$ so that the mixture density ρ_m and the mixture internal energy ε_m are defined by

$$\begin{cases} \rho_m = \alpha\rho_g^s + (1-\alpha)\rho_\ell^s, & \text{(1a)} \\ \rho_m\varepsilon_m = \alpha\rho_g^s\varepsilon_g^s + (1-\alpha)\rho_\ell^s\varepsilon_\ell^s, & \text{(1b)} \end{cases}$$

where ρ_g^s, ρ_ℓ^s, ε_g^s and ε_ℓ^s denote respectively vapour/liquid densities and internal energies at saturation. The enthalpy is connected to the internal energy by the relation $\rho h = \rho\varepsilon + p$ so that, when the pressure is the same in both phases, relation (1b) is equivalent to

$$\rho_m h = \alpha\rho_g^s h_g^s + (1-\alpha)\rho_\ell^s h_\ell^s, \tag{1b'}$$

where h_g^s, h_ℓ^s are respectively vapour/liquid enthalpies at saturation. Since we chose (h, p) as main variables, relations (1a) and (1b') provide the expression of the volume fraction:

$$\alpha(h, p) = \begin{cases} 0, & \text{if } h \leq h_\ell^s(p), \\ \dfrac{\rho_\ell^s(p)\cdot\left(h - h_\ell^s(p)\right)}{\left[\rho_g^s h_g^s - \rho_\ell^s h_\ell^s\right](p) - h\cdot\left[\rho_g^s - \rho_\ell^s\right](p)}, & \text{if } h_\ell^s(p) < h < h_g^s(p), \\ 1, & \text{if } h \geq h_g^s(p). \end{cases} \tag{2}$$

Density of two-phase media As a result of (1a) and (2), the density is expressed as a function of enthalpy h and pressure p:

$$\rho(h, p) = \begin{cases} \rho_\ell(h, p), & \text{if } h \leq h_\ell^s(p), \\ \rho_m(h, p) \overset{\text{def}}{=} \dfrac{\left[\rho_g^s\rho_\ell^s(h_g^s - h_\ell^s)\right](p)}{\left[\rho_g^s h_g^s - \rho_\ell^s h_\ell^s\right](p) - h\cdot\left[\rho_g^s - \rho_\ell^s\right](p)}, & \text{if } h_\ell^s(p) < h < h_g^s(p), \\ \rho_g(h, p), & \text{if } h \geq h_g^s(p). \end{cases} \tag{3}$$

The densities in pure phases ρ_ℓ and ρ_g will be expressed later (section 2.3).

Temperature of two-phase media The temperature in the mixture T^s is implicitly defined by the equation $G_\ell(p, T^s) = G_g(p, T^s)$ so that the temperature depends continuously on the enthalpy and on the pressure. It reads

$$T(h, p) = \begin{cases} T_\ell(h, p), & \text{if } h \leq h_\ell^s(p), \\ T^s(p), & \text{if } h_\ell^s(p) < h < h_g^s(p), \\ T_g(h, p), & \text{if } h \geq h_g^s(p). \end{cases} \tag{4}$$

We must emphasize that the function $h \mapsto T(h, p = p_0)$ cannot be inverted in the mixture zone for a constant pressure (as it is the case in the LMNC model).

5

Compressibility coefficient of two-phase media Computing the derivative of the density through the previous expression (3), we obtain for the compressibility coefficient

$$\beta(h,p) \stackrel{\text{def}}{=} -\frac{p}{\rho^2} \cdot \frac{\partial \rho}{\partial h}\bigg|_p = \begin{cases} \beta_\ell(h,p), & \text{if } h \leq h_\ell^s(p), \\ \beta_m(p) \stackrel{\text{def}}{=} p \cdot \dfrac{1/\rho_g^s(p) - 1/\rho_\ell^s(p)}{h_g^s(p) - h_\ell^s(p)} & \text{if } h_\ell^s(p) < h < h_g^s(p), \\ \beta_g(h,p), & \text{if } h \geq h_g^s(p). \end{cases} \tag{5}$$

The fact that the pressure is constant in the LMNC model implies the compressibility coefficient is constant in the mixture.

Remark 2.1. *Two facts must be underlined:*

- *Thanks to the Clausius-Clapeyron relation we notice that $\frac{\beta_m(p)}{p} = \frac{(T^s)'(p)}{T^s(p)}$ where $(T^s)'$ is the derivative of the coexistence curve $p \mapsto T^s(p)$;*

- *The density in the mixture can be written as*

$$\rho_m(h,p) = \frac{p/\beta_m(p)}{h - q_m(p)} \qquad with \qquad q_m(p) \stackrel{\text{def}}{=} \frac{\rho_g^s(p)h_g^s(p) - \rho_\ell^s(p)h_\ell^s(p)}{\rho_g^s(p) - \rho_\ell^s(p)}. \tag{6}$$

Hence when p is a constant, the density in the mixture can be written as a Stiffened Gas law [3].

- *Let us underline that α, ρ and T given resp. by (2), (3) and (4) are continuous functions of (h,p) unlike β which is discontinuous at the saturation points $h_\ell^s(p)$ and $h_g^s(p)$. Such discontinuities arise for any quantity derived from a differentiation with respect to h and/or p of α, ρ or T, like the speed of sound (see (8)).*

Viscosities and thermal conductivity Let μ and η be respectively the dynamic and bulk viscosities, and λ the thermal conductivity. In this study, our modelling assumptions make us work with variables (h,p) on which both coefficients thus depend continuously.

More precisely, for $\zeta \in \{\mu, \lambda\}$:

$$\zeta(h,p) = \begin{cases} \zeta_\ell(h,p), & \text{if } h \leq h_\ell^s(p), \\ \zeta_m(h,p) \stackrel{\text{def}}{=} \alpha(h,p)\zeta_g^s(p) + \big(1 - \alpha(h,p)\big)\zeta_\ell^s(p), & \text{if } h_\ell^s(p) < h < h_g^s(p), \\ \zeta_g(h,p), & \text{if } h \geq h_g^s(p), \end{cases} \tag{7}$$

where $\zeta_\kappa^s(p) \stackrel{\text{def}}{=} \zeta_\kappa\big(h_\kappa^s(p), p\big)$. As for the bulk viscosity, we take $\eta = -\frac{2}{3}\mu$ under the Stokes hypothesis.

Speed of sound of two-phase media The speed of sound will be needed to evaluate the Mach number in the differential system. It is given by

$$c^*(h,p) \stackrel{\text{def}}{=} \sqrt{\frac{\partial p}{\partial \rho}\bigg|_S} = \frac{1}{\sqrt{\frac{1}{\rho(h,p)}\frac{\partial \rho}{\partial h}(h,p) + \frac{\partial \rho}{\partial p}(h,p)}} = \begin{cases} c_\ell^*(h,p), & \text{if } h \leq h_\ell^s(p), \\ c_m^*(h,p), & \text{if } h_\ell^s(p) < h < h_g^s(p), \\ c_g^*(h,p), & \text{if } h \geq h_g^s(p), \end{cases} \tag{8}$$

where the speed of sound in the mixture is given by

$$\left(\frac{1}{c_m^*}\right)^2(h,p) = \frac{1}{\rho_m(h,p)}\frac{\partial \rho_m(h,p)}{\partial h}\bigg|_p + \frac{\partial \rho_m(h,p)}{\partial p}\bigg|_h$$

$$\stackrel{(6)}{=} \frac{1}{h - q_m(p)}\left[\frac{1}{\beta_m(p)} - \frac{p}{\beta_m(p)}\left(\frac{\beta_m'(p)}{\beta_m(p)} - \frac{q_m'(p)}{h - q_m(p)}\right) - 1\right]$$

with

$$\beta_m'(p) = \frac{\beta_m(p)}{p}\left(1 - p\frac{(h_g^s)'(p) - (h_\ell^s)'(p)}{h_g^s(p) - h_\ell^s(p)}\right) - p\frac{\frac{(\rho_g^s)'(p)}{(\rho_g^s(p))^2} - \frac{(\rho_\ell^s)'(p)}{(\rho_\ell^s(p))^2}}{h_g^s(p) - h_\ell^s(p)},$$

$$q_m'(p) = \frac{1}{\rho_g^s(p) - \rho_\ell^s(p)}\left((\rho_g^s h_g^s)'(p) - (\rho_\ell^s h_\ell^s)'(p) - q_m(p)\left((\rho_g^s)'(p) - (\rho_\ell^s)'(p)\right)\right),$$

$$(\rho_\kappa^s h_\kappa^s)'(p) = (\rho_\kappa^s)'(p)h_\kappa^s(p) + (h_\kappa^s)'(p)\rho_\kappa^s(p),$$

6

p [MPa]	ρ_ℓ^s [kg·m^{-3}]	h_ℓ^s [kJ·kg^{-1}]	ρ_g^s [kg·m^{-3}]	h_g^s [kJ·kg^{-1}]
$p_{-1} = 15.499$	594.397161363	1629.84051905	101.919399943	2596.14861770
$p_0 = 15.500$	594.378648626	1629.87998125	101.930084802	2596.11873446
$p_1 = 15.501$	594.360134886	1629.91944396	101.940770824	2596.08884821

Table 1: Data on saturation curve to compute $(\rho_\ell^s)'$, $(\rho_g^s)'$, $(h_\ell^s)'$ and $(h_g^s)'$ depending on p. Values for water [19]

where $(\rho_\kappa^s)'$ and $(h_\kappa^s)'$ are the derivatives of $p \mapsto \rho_\kappa^s(p)$ and $p \mapsto h_\kappa^s(p)$. When one uses analytical EOS in pure phases, we can differentiate these relations to obtain those derivatives (as in [3] with the stiffened gas law). In the present case, as we use tabulated values in pure phases, $(\rho_\kappa^s)'$ and $(h_\kappa^s)'$ are approximated by centered finite differences:

$$(\rho_\kappa^s)'(p_0) = \frac{\rho_\kappa^s(p_{-1}) - \rho_\kappa^s(p_1)}{p_{-1} - p_1}, \qquad (\rho_\kappa^s h_\kappa^s)'(p_0) = \frac{\rho_\kappa^s(p_{-1})h_\kappa^s(p_{-1}) - \rho_\kappa^s(p_1)h_\kappa^s(p_1)}{p_{-1} - p_1},$$

where p_i, $\rho_\kappa^s(p_i)$ and $h_\kappa^s(p_i)$, $i = -1, 0, 1$, are obtained experimentally (see Table 1 for the pressure of interest $p_0 = 15.5$ MPa).

Remark 2.2. *For the speed of sound in the mixture, in [3] we have the following equivalent expression:*

$$\left(\frac{1}{c_m^*}\right)^2 (h, p) =$$

$$\frac{[-\alpha(h,p)(\rho_g^s)'(p) - (1 - \alpha(h,p))(\rho_\ell^s)'(p)]q_m(p) + \alpha(h,p)(\rho_g^s h_g^s)'(p) + (1 - \alpha(h,p))(\rho_\ell^s h_\ell^s)'(p))(\rho_\ell^s)'(p) - 1}{h - q_m(p)}.$$

In [21, 25], another equivalent expression is used:

$$\left(\frac{1}{c_m^*}\right)^2 (h, p) =$$

$$\rho_m(h, p) \left(\frac{\alpha(h,p)}{\rho_g^s(p)(c_g^s)^2(p)} + \frac{1 - \alpha(h,p)}{\rho_\ell^s(p)(c_\ell^s)^2(p)} + T^s(p) \left(\alpha(h,p)\rho_g^s(p)\gamma_g c_{v_g}\chi_g^2(p) + (1 - \alpha(h,p))\rho_\ell^s(p)\gamma_\ell c_{v_\ell}\chi_\ell^2(p) \right) \right)$$

where $\chi_\kappa(h, p) = \frac{\beta_\kappa(h,p) - \beta_m(p)}{p}$ and $(c_\kappa^*)^s(p) = c_\kappa^*(h_\kappa^s(p), p)$ is the speed of sound of the pure phase κ at saturation. Note that $c_m^*(h_\kappa^s(p), p) < c_\kappa^*(h_\kappa^s(p), p)$, see for example [11, 20].

In the following section we detail how to express pure phase functions $(h, p = p_0) \mapsto (\rho_\kappa, T_\kappa, c_\kappa^*, \beta_\kappa, \mu_\kappa, \lambda_\kappa, c_{p_\kappa})$.

2.3 Construction of the EOS in pure phases

As mentioned above, the use of usual analytical EOS is restricted to some regimes and is not relevant in our study (Figure 1). Given values provided in tables, we rather construct polynomial functions approximating thermodynamic variables.

The PDE model presented in Section 3.1 is characterised by a constant thermodynamic pressure which is a consequence of the low Mach assumption. We underline that the pressure in normal situation in a PWR [7] is about $p_0 = 15.5$ MPa. For all these reasons, we do not need the whole table but only values related to pressure p_0 (see Table 2 for some values of variables $h, \rho, T, c^*, \mu, \lambda, c_p$).[2] The method then consists in constructing approximation functions $h \mapsto \left(\widetilde{\rho_\kappa}, \widetilde{T_\kappa}, \widetilde{c_\kappa^*}, \widetilde{\mu_\kappa}, \widetilde{\lambda_\kappa}, \widetilde{\frac{1}{c_{p_\kappa}}} \right)(h)$ fitting extracted values from the NIST tables [19] ($\kappa \in \{\ell, g\}$). More precisely, the sampling is done at the given pressure $p_0 = 15.5$ MPa with the temperature as reference:

$$T_i = T_1 + (i - 1)\Delta T, \qquad T_1 = 273.16 \text{ K and } \Delta T \approx 3.635 \text{ K}.$$

For each temperature T_i, values are measured and stored in the tables. The tables provided 96 values for the liquid phase and 107 values in the vapour phase. Given these pointwise values $\left(\rho_i, T_i, c_i^*, \mu_i, \lambda_i, \left(\frac{1}{c_p} \right)_i \right)$, we derive polynomial expressions $h \mapsto \left(\widetilde{\rho_\kappa}, \widetilde{T_\kappa}, \widetilde{c_\kappa^*}, \widetilde{\mu_\kappa}, \widetilde{\lambda_\kappa}, \widetilde{\frac{1}{c_{p_\kappa}}} \right)(h)$ approximating functions in each pure phase using a least-square regression technique. We mention that we interpolate $\frac{1}{c_p}$ instead of c_p due to oscillations appearing in the

---

[2]We recall that $c_p = \frac{\partial h}{\partial T}\big|_p$.

κ	h [kJ · kg^{-1}]	ρ_κ [kg · m^{-3}]	T_κ [K]	c_κ^* [m · s^{-1}]	μ_κ [Pa · s]	λ_κ [W · m^{-1} · K^{-1}]	c_{p_κ} [J · kg^{-1} · K^{-1}]
ℓ	15.608	1007.5	273.16	1427.4	1.7553×10^{-3}	0.569 60	4148.7
ℓ	30.678	1007.5	276.79	1445.0	1.5590×10^{-3}	0.576 04	4144.7
$\vdots$	$\vdots$	$\vdots$	$\vdots$	$\vdots$	$\vdots$	$\vdots$	$\vdots$
ℓ	1602.8	609.10	614.77	659.56	7.0252×10^{-5}	0.467 68	8187.3
ℓ	h_ℓ^s	594.38	T^s	621.43	6.8327×10^{-5}	0.458 47	8950
g	h_g^s	101.93	T^s	433.40	2.3108×10^{-5}	0.121 36	14 001
g	2602.6	101.06	618.41	435.61	2.3105×10^{-5}	0.119 77	13 491
$\vdots$	$\vdots$	$\vdots$	$\vdots$	$\vdots$	$\vdots$	$\vdots$	$\vdots$
g	3894.8	35.139	996.37	747.83	3.8357×10^{-5}	0.107 62	2529.9
g	3904.0	34.985	1000.0	749.37	3.8496×10^{-5}	0.108 08	2529

Table 2: Sample of water values [19] at $p_0 = 15.5\,\text{MPa}$

interpolation process for c_p at high enthalpy. Moreover, our choice is strengthened by the fact that $\frac{1}{c_p}$ is involved in the associated equations – see (10).

Unlike the previous variables, the compressibility coefficient β_κ is not referenced in the NIST tables. Here pointwise values $(\beta_\kappa)_i$ are computed by means of finite differences applied to approximate the derivative in Definition (5)

$$(\beta_\kappa)_i \approx \beta_\kappa(h_i, p_0) = -\frac{p_0}{\rho_i^2} \frac{\rho_{i+1} - \rho_{i-1}}{h_{i+1} - h_{i-1}}.$$

As previously, we then construct the fitting polynomial $h \mapsto \widetilde{\beta}(h)$ applying a least-square method to the resulting values $(\beta_\kappa)_i$. Let us mention that we could have computed $(\beta_\kappa)_i$ using the derivative of $h \mapsto \widetilde{\rho}(h)$. However the fitting procedure does not ensure the monotonicity of $h \mapsto \widetilde{\rho}(h)$ (hence the positivity of β) although the data (ρ_i, h_i) satisfy this requirement. We had rather used Taylor expansions in order to guarantee that $\beta > 0$. Likewise, we used tabulated values for $1/c_p$ instead of computing the derivative of $h \mapsto \widetilde{T}(h)$.[3]

We decided to increase the degree of the polynomial until a relative error of 10^{-4} is reached except if the convergence rate is too slow. The coefficients computed in the present paper are detailed in Tables 3 and 4 for the liquid phase and in Tables 5 and 6 for the vapour phase. We used normalised values for h (polynomials are expressed as functions of $\frac{h}{10^6}$) in order to avoid inaccuracies due to the order of magnitude of the enthalpy.

---

[3]Hence, there is no guarantee that $\widetilde{\beta} = -\frac{p_0}{\widetilde{\rho}^2} \frac{\partial \widetilde{\rho}}{\partial h}$ nor $\widetilde{\frac{1}{c_p}} = \frac{\partial \widetilde{T}}{\partial h}$.

N	$\widetilde{\rho}_\ell\left(\frac{h}{10^6}\right) = \sum_{i=0}^{N}\left(\frac{h}{10^6}\right)^i a_i$	$\widetilde{T}_\ell\left(\frac{h}{10^6}\right) = \sum_{i=0}^{N}\left(\frac{h}{10^6}\right)^i a_i$	$\widetilde{\beta}_\ell\left(\frac{h}{10^6}\right) = \sum_{i=0}^{N}\left(\frac{h}{10^6}\right)^i a_i$	$\widetilde{c^*}_\ell\left(\frac{h}{10^6}\right) = \sum_{i=0}^{N}\left(\frac{h}{10^6}\right)^i a_i$
	6	5	5	7
a_0	1007.663804	269.494756	-3.144415×10^{-4}	1408.715508
a_1	5.816753	239.176746	1.513681×10^{-2}	1285.276896
a_2	-362.121769	12.892175	-3.796005×10^{-2}	-3173.478514
a_3	402.251899	-28.445212	6.256348×10^{-2}	3477.989328
a_4	-346.462597	19.084606	-4.731887×10^{-2}	-2661.294781
a_5	163.929926	-7.561162	1.419670×10^{-2}	1158.792029
a_6	-34.293509			-222.506089
a_7				3.705771
$\|\text{relative error}\|_\infty$	1.932963×10^{-4}	2.981560×10^{-4}	0.237362	4.804380×10^{-4}

Table 3: Liquid phase: least-square regression coefficients for ρ, T, β and c^* at $p_0 = 15.5\,\mathrm{MPa}$

N	$\widetilde{\mu}_\ell\left(\frac{h}{10^6}\right) = \sum_{i=0}^{N}\left(\frac{h}{10^6}\right)^i a_i$	$\widetilde{\lambda}_\ell\left(\frac{h}{10^6}\right) = \sum_{i=0}^{N}\left(\frac{h}{10^6}\right)^i a_i$	$\widetilde{\frac{1}{c_p}}_\ell\left(\frac{h}{10^6}\right) = \sum_{i=0}^{N}\left(\frac{h}{10^6}\right)^i a_i$
	7	6	7
a_0	$1.887035985 \times 10^{-3}$	$5.590706836 \times 10^{-1}$	$2.411396483 \times 10^{-4}$
a_1	$-1.231330270 \times 10^{-2}$	$5.444196810 \times 10^{-1}$	$7.373142473 \times 10^{-6}$
a_2	$4.284555156 \times 10^{-2}$	$-6.056990203 \times 10^{-1}$	$-3.979053939 \times 10^{-5}$
a_3	$-8.533375202 \times 10^{-2}$	$-1.220393417 \times 10^{-1}$	$3.807563522 \times 10^{-5}$
a_4	$9.952851792 \times 10^{-2}$	$6.664649894 \times 10^{-1}$	$-5.278384866 \times 10^{-6}$
a_5	$-6.695156511 \times 10^{-2}$	$-5.166737011 \times 10^{-1}$	$-7.362604903 \times 10^{-5}$
a_6	$2.400317661 \times 10^{-2}$	$1.274930957 \times 10^{-1}$	$7.118550997 \times 10^{-5}$
a_7	$-3.546840761 \times 10^{-3}$		$-2.129646156 \times 10^{-5}$
$\|\text{relative error}\|_\infty$	$4.123091896 \times 10^{-2}$	$3.827235077 \times 10^{-3}$	$2.361683935 \times 10^{-3}$

Table 4: Liquid phase: least-square regression coefficients for μ, λ and c_p^{-1} at $p_0 = 15.5\,\mathrm{MPa}$

N	$\widetilde{\rho}_g\left(\frac{h}{10^6}\right) = \sum_{i=0}^{N}\left(\frac{h}{10^6}\right)^i a_i$	$\widetilde{T}_g\left(\frac{h}{10^6}\right) = \sum_{i=0}^{N}\left(\frac{h}{10^6}\right)^i a_i$	$\widetilde{\beta}_g\left(\frac{h}{10^6}\right) = \sum_{i=0}^{N}\left(\frac{h}{10^6}\right)^i a_i$	$\widetilde{c}^*_g\left(\frac{h}{10^6}\right) = \sum_{i=0}^{N}\left(\frac{h}{10^6}\right)^i a_i$
	4	4	6	4
a_0	$1414.830\,135$	$3167.047\,125$	$-1.496\,622$	$-1094.301\,040$
a_1	$-1044.100\,762$	$-2237.169\,444$	$0.732\,400$	$852.281\,489$
a_2	$264.354\,241$	$522.024\,090$	$0.268\,215$	$-98.148\,581$
a_3	$-21.164\,086$	$2.162\,368$	$-0.129\,772$	$-4.415\,234$
a_4	$0.318\,135$	$-6.538\,303$	$-1.622\,119 \times 10^{-2}$	$1.183\,168$
a_5			$1.149\,367 \times 10^{-2}$	
a_6			$-1.178\,786 \times 10^{-3}$	
$\|$relative error$\|_\infty$	$0.012\,704$	$7.288\,570 \times 10^{-4}$	$0.028\,350$	$6.112\,851 \times 10^{-4}$

Table 5: Vapor phase: least-square regression coefficients for ρ, T, β and c^* at $p_0 = 15.5\,\mathrm{MPa}$

N	$\widetilde{\mu}_g\left(\frac{h}{10^6}\right) = \sum_{i=0}^{N}\left(\frac{h}{10^6}\right)^i a_i$	$\widetilde{\lambda}_g\left(\frac{h}{10^6}\right) = \sum_{i=0}^{N}\left(\frac{h}{10^6}\right)^i a_i$	$\widetilde{\frac{1}{c_{p_g}}}\left(\frac{h}{10^6}\right) = \sum_{i=0}^{N}\left(\frac{h}{10^6}\right)^i a_i$
	4	4	6
a_0	$2.000\,227\,843 \times 10^{-4}$	$3.072\,101\,965$	$2.142\,054\,360 \times 10^{-3}$
a_1	$-1.626\,163\,794 \times 10^{-4}$	$-2.562\,163\,653$	$-1.589\,909\,728 \times 10^{-3}$
a_2	$4.492\,057\,340 \times 10^{-5}$	$7.216\,534\,878 \times 10^{-1}$	$-4.533\,788\,097 \times 10^{-4}$
a_3	$-2.771\,197\,243 \times 10^{-6}$	$-6.681\,266\,126 \times 10^{-2}$	$4.353\,213\,187 \times 10^{-4}$
a_4	$-2.002\,090\,217 \times 10^{-7}$	$6.046\,442\,269 \times 10^{-5}$	$9.252\,490\,506 \times 10^{-6}$
a_5			$3.757\,526\,958 \times 10^{-5}$
a_6			$4.913\,802\,546 \times 10^{-6}$
$\|$relative error$\|_\infty$	$3.584\,935\,953 \times 10^{-3}$	$2.121\,711\,706 \times 10^{-3}$	$3.091\,433\,051 \times 10^{-2}$

Table 6: Vapor phase: least-square regression coefficients for μ, λ and c_p^{-1} at $p_0 = 15.5\,\mathrm{MPa}$

	TAB [19]	SG [3]
h_ℓ^s	$1.629 \times 10^6 \, \mathrm{J \cdot K^{-1}}$	$1.627 \times 10^6 \, \mathrm{J \cdot K^{-1}}$
h_g^s	$2.596 \times 10^6 \, \mathrm{J \cdot K^{-1}}$	$3.004 \times 10^6 \, \mathrm{J \cdot K^{-1}}$
ρ_ℓ^s	$594.38 \, \mathrm{kg \cdot m^{-3}}$	$632.663 \, \mathrm{kg \cdot m^{-3}}$
ρ_g^s	$101.93 \, \mathrm{kg \cdot m^{-3}}$	$52.937 \, \mathrm{kg \cdot m^{-3}}$
T^s	$617 \, \mathrm{K}$	$654 \, \mathrm{K}$

Table 7: Values at saturation for $p_0 = 15.5 \, \mathrm{MPa}$.

	TAB [19]	SG [3]
β_ℓ	1.521×10^{-4} to 2.383×10^{-2}	8.769×10^{-3}
β_m	1.304×10^{-1}	1.949×10^{-1}
β_g	1.997×10^{-1} to 2.322×10^{-1}	3.007×10^{-1}
$(c^*)_\ell$	$621.43 \, \mathrm{m \cdot s^{-1}}$ to $1584.7 \, \mathrm{m \cdot s^{-1}}$	$1263.24 \, \mathrm{m \cdot s^{-1}}$ to $1942.17 \, \mathrm{m \cdot s^{-1}}$
$(c^*)_m$	$103.27 \, \mathrm{m \cdot s^{-1}}$ to $372.26 \, \mathrm{m \cdot s^{-1}}$	$186.69 \, \mathrm{m \cdot s^{-1}}$ to $578.88 \, \mathrm{m \cdot s^{-1}}$
$(c^*)_g$	$433.40 \, \mathrm{m \cdot s^{-1}}$ to $749.37 \, \mathrm{m \cdot s^{-1}}$	$647.07 \, \mathrm{m \cdot s^{-1}}$ to $897.61 \, \mathrm{m \cdot s^{-1}}$

Table 8: Orders of magnitude of some variables at $p_0 = 15.5 \, \mathrm{MPa}$

2.4 Tabulated values vs Stiffened Gas law

In a preliminary work [3], we supplemented the LMNC model with the Stiffened Gas law in each phase. The parameters of the SG law were tuned following [18] at $p_0 = 15.5 \, \mathrm{MPa}$ for temperatures close to saturation. However, by construction, this EOS is more relevant for low pressure states since the assumption of linearity of $h \mapsto T(h, p_0)$ is more questionable as the pressure increases.

This can be observed in Table 7 where there is a noticeable discrepancy between computed values from the SG law and measured values from [19]. In particular, the error upon the temperature at saturation is about 6% which may result in dramatic consequences as the computations provide a late vaporisation: indeed, for $p_0 = 15.5 \, \mathrm{MPa}$, the temperature at saturation provided in the NIST tables is equal to $617 \, \mathrm{K}$, and that computed with the Stiffened Gas law is equal to $654 \, \mathrm{K}$, (see Figure 1). We underline that the Stiffened Gas law was not designed for this range of temperature values.

Figures 4 show the accuracy of the interpolation process: points extracted from the NIST tables (legend NIST_κ) match the polynomial curves (solid curves) even if the least square method does not impose $\widetilde{\zeta}(h_i) = \zeta_i$, for $\zeta \in \{\rho, \lambda, \vartheta, \beta, \mu, \eta\}$. These curves are compared to the Stiffened Gas ones (legend SG_κ), and we notice quite different orders of magnitudes (see also Table 8) and even different monotonicities (see Figures 4c, 4d and 4e) of the compressibility coefficient, the speed of sound and the heat capacity.

We mention that there is no modelling for c_p in the mixture phase (Figure 4e) since

$$c_p = \left. \frac{\partial h}{\partial T} \right|_p$$

has no physical meaning at saturation: $h \mapsto T(h, p_0)$ is indeed constant in the mixture (see figures 2a and 3a).

3 Two-phase flow model

3.1 Equations

The LMNC model derived in [8] was mainly investigated under its non-conservative formulation [2,3,9]
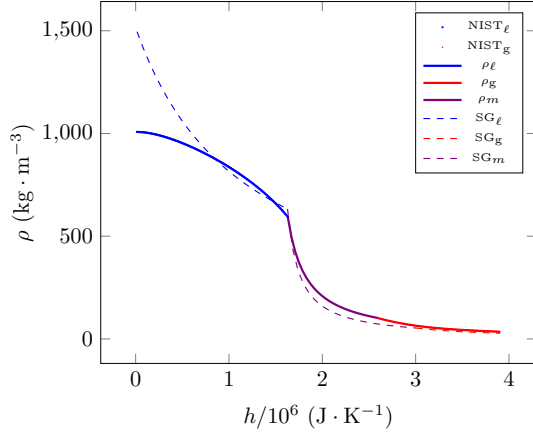
$$\begin{cases} \nabla \cdot \boldsymbol{u} = \dfrac{\beta(h, p_0)}{p_0} \left[\nabla \cdot \big(\lambda(h, p_0) \nabla T(h, p_0) \big) + \Phi \right], & \text{(9a)} \\[2mm] \rho(h, p_0) \times \left[\partial_t h + \boldsymbol{u} \cdot \nabla h \right] = \nabla \cdot \big(\lambda(h, p_0) \nabla T(h, p_0) \big) + \Phi, & (t, \boldsymbol{x}) \in \mathbb{R}^+ \times \Omega_d, & \text{(9b)} \\[2mm] \rho(h, p_0) \times \left[\partial_t \boldsymbol{u} + (\boldsymbol{u} \cdot \nabla) \boldsymbol{u} \right] - \nabla \cdot \sigma(\boldsymbol{u}) + \nabla \overline{p} = \rho(h, p_0) \boldsymbol{g}, & \text{(9c)} \end{cases}$$

for some bounded domain[4] $\Omega_d \subset \mathbb{R}^d$, $d \in \{1, 2\}$.
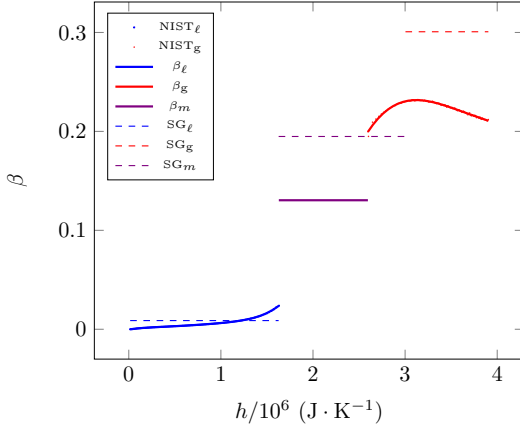
---

[4]Typically, in 1D, $\Omega_1 = [0, L_y]$ and $\boldsymbol{x} = y$, whereas in 2D $\Omega_2 = [0, L_x] \times [0, L_y]$ and $\boldsymbol{x} = (x, y)$.
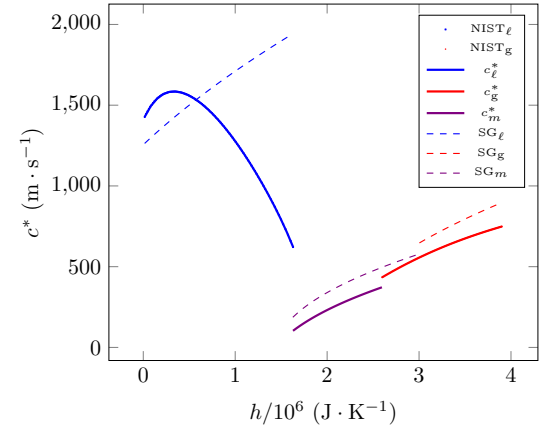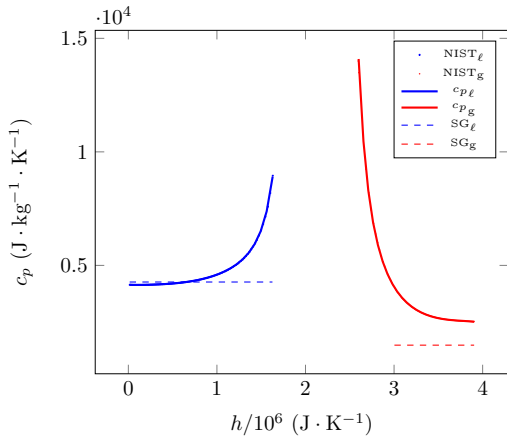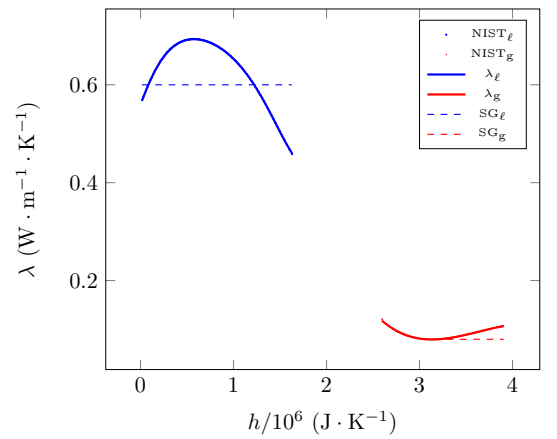
(a) Density.
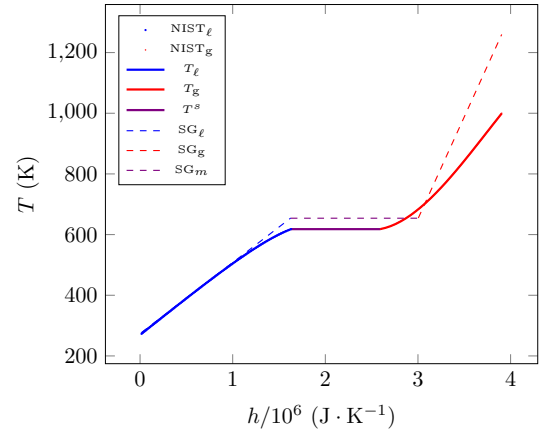
(b) Temperature.

(c) Compressibility coefficient.

(d) Speed of sound.

(e) Heat capacity.

(f) Thermal conductivity.

Figure 4: Thermodynamic variables as functions of the enthalpy at $p_0 = 15.5\,\mathrm{MPa}$

Let us specify the terms involved in this system: $\boldsymbol{u} = (u, v)$ and h denote respectively the velocity field and the enthalpy of the fluid.

The density $\rho = \rho(h, p_0)$, the thermal conductivity $\lambda = \lambda(h, p_0)$ and the compressibility coefficient $\beta(h, p_0)$ are related to the enthalpy through the equation of state. Actually, these functions are replaced by fitting polynomials $\widetilde{\rho}$, $\widetilde{\lambda}$ and $\widetilde{\beta}$ as explained in the previous section. So does the temperature $T = T(h, p_0)$ but we only use polynomial $\widetilde{T}$ as a postprocessing to depict the temperature. In particular, we do not differentiate the polynomial expression $h \mapsto \widetilde{T}(h)$ in Eqs. (9a) and (9b) but we rather use the thermodynamic relation

$$\nabla T(h, p_0) = \vartheta(h, p_0) \nabla h, \qquad \text{with} \qquad \vartheta(h, p_0) = \begin{cases} \vartheta_\ell(h, p_0) \overset{\text{def}}{=} \dfrac{1}{c_{p_\ell}(h, p_0)}, & \text{if } h \leq h_\ell^s(p_0), \\[2mm] \vartheta_m(h, p_0) \equiv 0, & \text{if } h_\ell^s(p_0) < h < h_g^s(p_0), \\[2mm] \vartheta_g(h, p_0) \overset{\text{def}}{=} \dfrac{1}{c_{p_g}(h, p_0)}, & \text{if } h \geq h_g^s(p_0). \end{cases} \tag{10}$$

The temperature beeing constant within the mixture area, $\vartheta_m(h, p_0) \equiv 0$.

The power density $\Phi = \Phi(t, \boldsymbol{x})$ is a given function of time and space modelling the heating of the coolant fluid due to the fission reactions in the nuclear core. Finally, $\boldsymbol{g}$ is the gravity field and $\sigma(\boldsymbol{u})$ models viscous effects: the classic internal friction in the fluid, and also the friction on the fluid due to technological devices in the nuclear core (*e.g.* the friction on the fluid due to the fuel rods):

$$\sigma(\boldsymbol{u}) = \mu(h, p_0) \times \left(\nabla \boldsymbol{u} + (\nabla \boldsymbol{u})^T\right) + \eta(h, p_0) \times (\nabla \cdot \boldsymbol{u}) \, \mathbb{I}.$$

The very expression of the viscous term was not important in the 1D framework as Eq. (9c) was a post-processing leading to the computation of $\bar{p}$ ([3]). This is no more the case in higher dimensions where the latter equation is a real part of the system. We recall that we take $\eta = -\frac{2}{3}\mu$ (Stokes hypothesis).

The conservative counterpart of System (9) is

$$\begin{cases} \partial_t \rho(h, p_0) + \nabla \cdot \left(\rho(h, p_0) \boldsymbol{u}\right) = 0, & \text{(11a)} \\[2mm] \partial_t \left(\rho(h, p_0) h\right) + \nabla \cdot \left(\rho(h, p_0) h \boldsymbol{u}\right) = \nabla \cdot \left(\lambda(h, p_0) \nabla T(h, p_0)\right) + \Phi, & (t, \boldsymbol{x}) \in \mathbb{R}^+ \times \Omega_d, \quad \text{(11b)} \\[2mm] \partial_t \left(\rho(h, p_0) \boldsymbol{u}\right) + \nabla \cdot \left(\rho(h, p_0) \boldsymbol{u} \otimes \boldsymbol{u}\right) - \nabla \cdot \sigma(\boldsymbol{u}) + \nabla \bar{p} = \rho(h, p_0) \boldsymbol{g}. & \text{(11c)} \end{cases}$$

The reader can refer to [3, Sect. 1.3] for more details upon equivalent formulations under smoothness assumptions. We must also emphasize that Model (9) is characterised by two pressure fields, which is classic in low Mach number approaches: the *thermodynamic pressure* p_0 is involved in the equation of state and the *dynamic pressure* $\bar{p}$ appears in Equation (9c). This pressure decomposition results from the filtering out the acoustic waves which are no more involved in System (9). Compared to its "parent" model (Euler or Navier-Stokes equations whether taking into account of viscosity effects or not), it is resulting from an asymptotic expansion w.r.t. the Mach number. As a consequence, System (9) has a different mathematical structure which may be easier to deal with.

We must underline that Equation (9b), which is of parabolic type in pure phases, degenerates to a hyperbolic equation in the mixture as the second order derivative vanishes – see (10). This must be ensured at the discrete level: the numerical scheme should be consistent with both parabolic and hyperbolic continuous counterparts.

3.2 Boundary conditions

Boundary conditions (BC) are specified in 2D ($\Omega_2 = [0, L_x] \times [0, L_y]$ where the vertical variable is y, see Fig. 5). We also make a few remarks about 1D BC prescribed in earlier works.

- The fluid is injected at the bottom $y = 0$ of the core at a given enthalpy h_e and at a given vertical flow rate D_e:
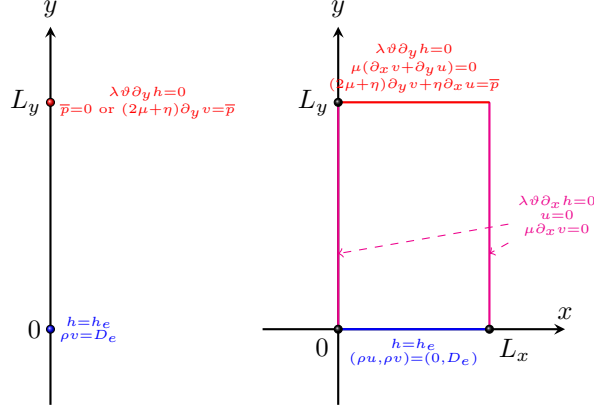
$$h(t, x, 0) = h_e(t, x), \tag{12a}$$

$$(\rho \boldsymbol{u})(t, x, 0) = \left(0, D_e(t, x)\right). \tag{12b}$$

  The vertical entrance velocity $v_e(t, x)$ applied at $y = 0$ is deduced from the relation $v_e(t, x) = D_e(t, x)/\rho_e(t, x)$ where $\rho_e = \rho(h_e, p_0)$.

  An alternative consists in prescribing both density and flow rate:

$$\rho(t, x, 0) = \rho_e(t, x), \tag{12a'}$$

$$(\rho \boldsymbol{u})(t, x, 0) = \left(0, D_e(t, x)\right). \tag{12b'}$$

(a) Domain Ω_1 (b) Domain Ω_2

Figure 5: Domain Ω_d, $d \in \{1, 2\}$ and boundary conditions

	$10^{-6}\widetilde{h}_\ell(10^{-2}\rho) = \sum\limits_{i=0}^{N} a_i(10^{-2}\rho)^i$	$10^{-6}\widetilde{h}_g(10^{-2}\rho) = \sum\limits_{i=0}^{N} a_i(10^{-2}\rho)^i$
N	8	4
a_0	$-5.004\,928\,223$	$8.414\,761\,047$
a_1	$2.099\,897\,820$	$-23.365\,457\,87$
a_2	$-7.860\,797\,723 \times 10^{-2}$	$40.116\,439\,16$
a_3	$4.795\,234\,627 \times 10^{-3}$	$-32.850\,083\,53$
a_4	$-1.342\,278\,527 \times 10^{-2}$	$10.294\,469\,16$
a_5	$3.050\,674\,531 \times 10^{-3}$	
a_6	$-3.191\,673\,091 \times 10^{-4}$	
a_7	$1.868\,583\,740 \times 10^{-5}$	
a_8	$-5.130\,646\,869 \times 10^{-7}$	

Table 9: Regression coefficients of $\rho \mapsto \widetilde{h}(\rho)$ for the computation of boundary conditions at the bottom of the domain

In that case, we need to invert the EOS to compute h_e from ρ_e. Rather than inverting the polynomial function $h \mapsto \widetilde{\rho}(h)$ in pure phases, we fit values of the enthalpy to construct $\rho \mapsto \widetilde{h}(\rho)$ applying the same procedure as in Section 2.3.[5] In the mixture, we directly invert the analytical expression $h \mapsto \rho_m(h, p_0)$ in (3). Coefficients of the polynomials $\widetilde{h}_\kappa$ are given in Table 9 (see also Figure 6).

- As for the temperature, we impose adiabatic conditions on all boundaries, except for the entry:

$$\lambda(h, p_0)\nabla T \cdot \boldsymbol{n}(t, 0, y) = \lambda(h, p_0)\nabla T \cdot \boldsymbol{n}(t, L_x, y) = 0, \qquad \text{[lateral walls]} \qquad (12\text{c})$$
$$\lambda(h, p_0)\nabla T \cdot \boldsymbol{n}(t, x, L_y) = 0. \qquad \text{[top]} \qquad (12\text{d})$$

- On the lateral walls we consider Robin conditions on the velocity:

$$(\boldsymbol{u} \cdot \boldsymbol{n})(t, 0, y) = (\boldsymbol{u} \cdot \boldsymbol{n})(t, L_x, y) = 0, \qquad (12\text{e})$$
$$\sigma(\boldsymbol{u})\boldsymbol{n} \cdot \boldsymbol{\tau}(t, 0, y) = \sigma(\boldsymbol{u})\boldsymbol{n} \cdot \boldsymbol{\tau}(t, L_x, y) = 0. \qquad (12\text{f})$$

- Finally, at the top of the core, we consider a free outflow

$$\big[\sigma(\boldsymbol{u})\boldsymbol{n} - \overline{p}\boldsymbol{n}\big](t, x, L_y) = \boldsymbol{0}. \qquad (12\text{g})$$

The corresponding BC for the "parent model" (Navier-Stokes for a compressible fluid) is[6]

$$\big[\sigma(\boldsymbol{u})\boldsymbol{n} - p\boldsymbol{n}\big](t, x, L_y) = -p_0\boldsymbol{n}. \qquad (12\text{g'})$$

---

[5] Hence the identity $\widetilde{\rho}\big(\widetilde{h}(\rho_i)\big) = \rho_i$ is not verified exactly.

[6] The physical pressure field p is recovered from the low Mach number model by $p = p_0 + \overline{p}$. Thus $\overline{p} = \mathcal{O}(\mathcal{M}^2)$ is a perturbation around the mean value p_0.
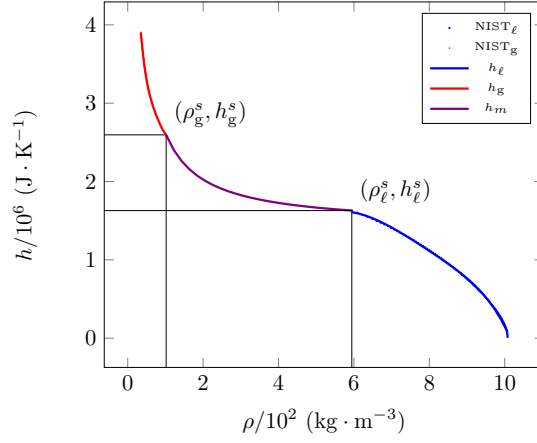
Figure 6: Plot of the EOS $\rho \mapsto \widetilde{h}(\rho)$ for the computation of boundary conditions at the bottom of the domain

Remark 3.1. *When viscosity is involved, BC* (12g) *does not match the boundary condition we considered in previous works [2, 3] which was*

$$\overline{p}(t, x, L_y) = 0.$$

Indeed, in 1D, the asymptotic expansion with the Mach number not only filters out the acoustic waves but it also changes the nature of the equations through the generation of two pressure fields. Eq. (9c) *decouples from the others and becomes an ODE upon $\overline{p}$ while in higher dimensions, the decoupling does not occur: Eq.* (9c) *is then a second-order PDE upon $(\boldsymbol{u}, \overline{p})$.*

Nevertheless, we can wonder about the signification of pressure p_0 in (12g'). *In the primary circuit of a PWR, there is a pressuriser at the exit of the core which maintains the water at high pressure. p_0 can thus be interpreted as the imposed pressure except that it is not imposed at the exit of the core but further in the circuit at a position $L_y + \epsilon$. The domain $[L_y, L_y + \epsilon]$ is modelled as an inviscid fluid – see the right hand side in* (12g') *– without heating process ($\Phi = 0$). We may think that ϵ goes to 0 as the Mach number does.*

3.3 Assumptions

For the problem to be well-posed, we impose some assumptions upon the data. We first suppose that physical data satisfy:

Hypothesis 3.1.

1. *For all $(t, \boldsymbol{x}) \in \mathbb{R}^+ \times \Omega_d$, $\Phi(t, \boldsymbol{x})$ is non-negative.*

2. *p_0 is a positive constant.*

The first assumption characterizes the fact that we study a nuclear core where the coolant fluid is heated. As for the boundary conditions, we choose:

Hypothesis 3.2.

1. *For all $(t, \boldsymbol{x}) \in \mathbb{R}^+ \times \Omega_d$, $D_e(t, \boldsymbol{x})|_{y=0}$ is non-negative.*

2. *h_e is such that ρ_e is well-defined and positive.*

In a nuclear power plant of PWR or BWR type, the flow is *upward*, which implies Hyp. 3.2.1. The second assumption means that h_e lies in the domain of definition of the EOS $h \mapsto \rho(h, p_0)$.

We finally make the following modelling hypothesis which somehow restricts the range of experiments as we cannot predict the orientation of the output velocity field.

Hypothesis 3.3. *The velocity field is outgoing, i.e. $\boldsymbol{u} \cdot \boldsymbol{n}(t, \boldsymbol{x})|_{y=L_y} > 0$ for all $(t, \boldsymbol{x}) \in \mathbb{R}^+ \times \Omega_d$.*

This hypothesis is necessary as no Dirichlet BC is imposed at the exit of the core upon the enthalpy. It thus induces that no downward flow (recirculation) occurs at the exit. In dimension 1, Hyp. 3.3 is a direct consequence of Hyps. 3.1 and 3.2 and of the positivity of β; in dimensions 2 and 3, Hyp. 3.3 must be stated.

4 Numerical schemes

The main goal of deriving low Mach number models relies on the quest for faster numerical treatments without significant loss of physical content. This is obviously achieved in dimension 1: Eq. (9c) is decoupled from the others which means it suffices to compute h and v to determine all other unknowns. Our numerical strategy in 1D – based on finite differences – is outlined in § 4.1. In higher dimensions, the overall coupling requires a more flexible method, for instance finite elements as described in § 4.2.

We introduced global functions $h \mapsto \zeta(h, p_0)$ defined piecewise by modelling expressions in the mixture (Section 2.2) and by equations of state in pure phases. We denote by $\widetilde{\zeta}(h)$ their approximation by means of the fitting procedure described in Section 2.3:

$$\widetilde{\zeta}(h) = \begin{cases} \widetilde{\zeta_\ell}(h), & \text{if } h \leq h_\ell^s(p_0), \\ \zeta_m(h, p_0), & \text{if } h_\ell^s(p_0) < h < h_g^s(p_0), \\ \widetilde{\zeta_g}(h), & \text{if } h \geq h_g^s(p_0), \end{cases}$$

for $\zeta \in \{\rho, \lambda, \vartheta, \beta, \mu, \eta\}$. We recall that $\rho, \lambda, \beta, \mu, \eta$ are defined in § 2.2 and ϑ in (10).

We chose to investigated the influence of thermal conduction in 2D, thus we only take it into account in the 2D-scheme.

4.1 1D-scheme

Without phase change and thermal conduction and with the Stiffened Gas law, the right hand side in (9a) is independent of the unknowns and the 1D velocity field can be directly recovered. As soon as tabulated values are considered, h and v are coupled but the method of characteristics enables to solve Equation (9b) using only values of the velocity field at the previous time step. The divergence constraint is then treated. When thermal conduction is involved, the difference is that the nature of Equation (9b) is modified in the pure phases where it turns parabolic. We do not present here the resulting numerical strategy for $\lambda \neq 0$ in dimension 1 (see [4] for more details) but rather focus on taking into account the tabulated law without thermal conduction.

To go into details, we recall some previous works. To approximate the solution of Equation (9b), we applied in [2] a third-order numerical method of characteristics (MOC – see [24]). A complete description of the scheme is provided in [3], as well as proofs of robustness of the algorithm (positivity of density, stability). In the sequel, we focus on modifications to adapt this scheme to tabulated EOS.

Given $\Delta y > 0$ and $\Delta t > 0$, we consider a uniform Cartesian grid $\{y_i = i\Delta y\}_{0 \leq i \leq N+1}$ such that $y_0 = 0$ and $y_{N+1} = L_y$ as well as a time discretisation $\{t^n = n\Delta t\}_{n \geq 0}$. Unknowns are co-located at the nodes of the mesh. We set the initial values $v_i^0 = v^0(y_i)$ and $h_i^0 = h^0(y_i)$ for $i = 0, \dots, N+1$.

Equation (9b) can be written as

$$\begin{cases} \dfrac{\mathrm{d}\chi}{\mathrm{d}\tau} = v\big(\tau, \chi(\tau; t, y)\big), \\ \chi(t; t, y) = y, \end{cases} \qquad \frac{\mathrm{d}}{\mathrm{d}\tau}\big[h\big(\tau, \chi(\tau; t, y)\big)\big] = \frac{\Phi\big(\tau, \chi(\tau; t, y)\big)}{\widetilde{\rho}\big(h\big(\tau, \chi(\tau; t, y)\big)\big)}. \tag{13}$$

To compute the numerical solution $(h_i^{n+1})_{0 \leq i \leq N+1}$, we set $t = t^{n+1}$ and $y = y_i$ in (13). Let ξ_i^n be the numerical approximation of $\chi(t^n; t^{n+1}, y_i)$. The advantage of the numerical method described in [24] is that the computation of ξ_i^n only involves the velocity at time t^n.

The scheme reads

$$h_i^{n+1} - \widehat{h}_i^n = \delta \frac{\hat{\Phi}_i^n}{\widetilde{\rho}(\widehat{h}_i^n)}, \tag{14}$$

where δ, $\widehat{h}_i^n$ and $\hat{\Phi}_i^n$ are defined depending on the sign of ξ_i^n (see Figs. 7):

- If $\xi_i^n > 0$ (see Fig. 7a), we integrate Eq. (13) over $[t^n, t^{n+1}]$ and we take $\delta = \Delta t$, $\hat{\Phi}_i^n = \Phi(t^n, \xi_i^n)$ and $\widehat{h}_i^n$ is a 2nd-order approximation of $h(t^n, \xi_i^n)$ (see [3]);

- If $\xi_i^n \leq 0$ (see Fig. 7b), let $t_{i,n}^*$ be the time such that $\chi(t_{i,n}^*; t^{n+1}, y_i) = 0$. We integrate Eq. (13) over $[t_{i,n}^*, t^{n+1}]$ and we take $\delta = t^{n+1} - t_{i,n}^*$, $\hat{\Phi}_i^n = \Phi(t_{i,n}^*, 0)$ and $\widehat{h}_i^n = h_e(t_{i,n}^*)$ applying BC (12a).

Once the enthalpy is computed, we can explicitly integrate Eq. (9a) to determine the velocity field and then Eq. (9c) to compute the dynamic pressure field. In this version of the algorithm, any equation of state can be incorporated and is involved in the computation of the density in (14).

In the same spirit as the INTMOC scheme was designed in [3], we could also write ODE (13) as

$$\frac{\mathrm{d}}{\mathrm{d}\tau}\left[\widetilde{R}\big(h\big(\tau, \chi(\tau; t, y)\big)\big)\right] = \Phi\big(\tau, \chi(\tau; t, y)\big)$$
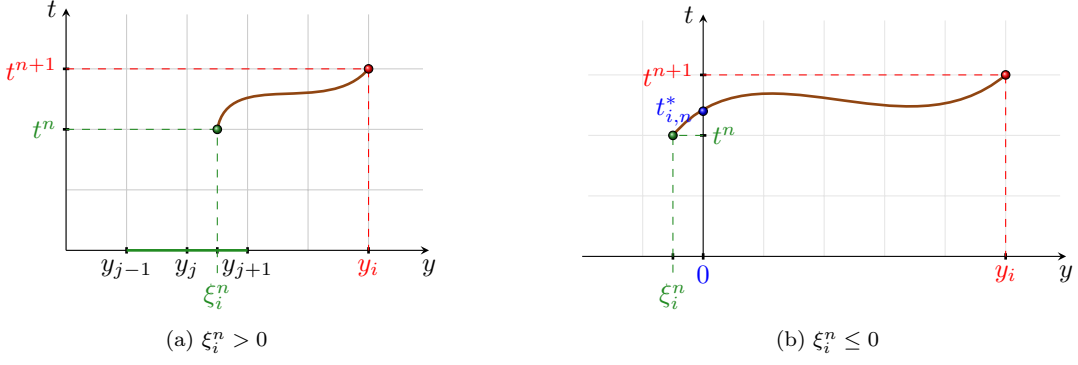
Figure 7: Numerical method of characteristics

where $\widetilde{R}$ is a polynomial such that $\widetilde{R}' = \widetilde{\rho}$ in order to make the scheme more accurate (since the right hand side does not depend on h henceforth). It is easily achievable as the coefficients of polynomial $\widetilde{\rho}$ are computed prior to the overall algorithm. The issue lies in the fact that unlike the stiffened gas case where R is easily invertible, the inversion of a 6th- or 7th-degree polynomial is not very accurate. This is why we restrict our study to Scheme (14).

4.2 2D-scheme

In higher dimensions, the decoupling no longer occurs but algorithms relying on the method of characteristics can still be considered. This feature is embedded in the Finite-Element software `FreeFem++` through the function `convect`. For reasons highlighted in Remark 4.1, we do not consider Equation (9a) as such but under the equivalent form

$$\nabla \cdot \boldsymbol{u} = \frac{\beta(h, p_0)\rho(h, p_0)}{p_0} \left[\partial_t h + \boldsymbol{u} \cdot \nabla h\right]. \tag{9a'}$$

Applying the method of characteristics to discretise the convection operators, the weak formulation reads

"**At time t^{n+1}, find** $(\boldsymbol{u}^{n+1}, h^{n+1}, \overline{p}^{n+1}) \in (\boldsymbol{u}_e + \mathcal{U}) \times (h_e + \mathcal{H}) \times \mathrm{L}^2(\Omega_2)$ **such that**

$$\iint_{\Omega_2} \nabla \cdot \boldsymbol{u}^{n+1} p_{\text{test}} \, \mathrm{d}\boldsymbol{x} = \iint_{\Omega_2} \frac{\widetilde{\beta}(h^n)\widetilde{\rho}(h^n)}{p_0} \frac{h^{n+1} - h^n(\boldsymbol{\xi}^n)}{\Delta t} p_{\text{test}} \, \mathrm{d}\boldsymbol{x}, \qquad\qquad \forall\, p_{\text{test}} \in \mathrm{L}^2(\Omega_2),$$

$$\iint_{\Omega_2} \widetilde{\rho}(h^n) \frac{h^{n+1} - h^n(\boldsymbol{\xi}^n)}{\Delta t} h_{\text{test}} \, \mathrm{d}\boldsymbol{x} = \iint_{\Omega_2} \Phi(t^{n+1}, \cdot) h_{\text{test}} \, \mathrm{d}\boldsymbol{x} - \iint_{\Omega_2} \widetilde{\lambda}(h^n)\widetilde{\vartheta}(h^n)\nabla h^{n+1} \cdot \nabla h_{\text{test}} \, \mathrm{d}\boldsymbol{x}, \quad \forall\, h_{\text{test}} \in \mathcal{H},$$

$$\iint_{\Omega_2} \widetilde{\rho}(h^n) \frac{\boldsymbol{u}^{n+1} - \boldsymbol{u}^n(\boldsymbol{\xi}^n)}{\Delta t} \cdot \boldsymbol{u}_{\text{test}} \, \mathrm{d}\boldsymbol{x} + \iint_{\Omega_2} \frac{\widetilde{\mu}(h^n)}{2} \left(\nabla \boldsymbol{u}^{n+1} + (\nabla \boldsymbol{u}^{n+1})^T\right) :: \left(\nabla \boldsymbol{u}_{\text{test}} + \nabla \boldsymbol{u}_{\text{test}}^T\right) \, \mathrm{d}\boldsymbol{x}$$

$$+ \iint_{\Omega_2} \widetilde{\eta}(h^n) (\nabla \cdot \boldsymbol{u}^{n+1})(\nabla \cdot \boldsymbol{u}_{\text{test}}) \, \mathrm{d}\boldsymbol{x} - \iint_{\Omega_2} \overline{p}^{n+1} \nabla \cdot \boldsymbol{u}_{\text{test}} \, \mathrm{d}\boldsymbol{x} = \iint_{\Omega_2} \widetilde{\rho}(h^n) \boldsymbol{g} \cdot \boldsymbol{u}_{\text{test}} \, \mathrm{d}\boldsymbol{x}, \qquad \forall\, \boldsymbol{u}_{\text{test}} \in \mathcal{U},"$$

where

$$\mathcal{H} = \left\{\theta \in \mathrm{H}^1(\Omega_2) \colon \theta(x, 0) = 0\right\},$$

$$\mathcal{U} = \left\{\boldsymbol{v} \in \left(\mathrm{H}^1(\Omega_2)\right)^2 \colon \boldsymbol{v}(x, 0) = \boldsymbol{0},\ \boldsymbol{v} \cdot \boldsymbol{n}(0, y) = \boldsymbol{v} \cdot \boldsymbol{n}(L_x, y) = 0\right\}.$$

Similarly to § 4.1, $\boldsymbol{\xi}^n$ is a numerical approximation of $\boldsymbol{\xi}(t^n; t^{n+1}, \boldsymbol{x})$ where $\boldsymbol{\xi}$ is the solution of the 2D-counterpart of the characteristic equation (13).

We do not give more details either about the mathematical content or the numerical treatment since the problem is simulated by means of `FreeFem++` [16], which solves directly the weak formulation given above.

Remark 4.1. *We must mention that the replacement of Equation (9a) by (9a') in the weak formulation above can be surprising. A direct integration of (9a) with appropriate integrations by parts would give*

$$\iint_{\Omega_2} \nabla \cdot \boldsymbol{u}^{n+1} p_{test} \, \mathrm{d}\boldsymbol{x} = \iint_{\Omega_2} \frac{\widetilde{\beta}(h^n) p_{test}}{p_0} \Phi \, \mathrm{d}\boldsymbol{x}$$

$$+ \int_{\partial\Omega_\ell(t^n)} \frac{\widetilde{\beta}_\ell(h^n) p_{test}}{p_0} \widetilde{\lambda}_\ell(h^n)\widetilde{\vartheta}_\ell(h^n)\nabla h^{n+1} \cdot \boldsymbol{n} \, \mathrm{d}\varsigma + \int_{\partial\Omega_g(t^n)} \frac{\widetilde{\beta}_g(h^n) p_{test}}{p_0} \widetilde{\lambda}_g(h^n)\widetilde{\vartheta}_g(h^n)\nabla h^{n+1} \cdot \boldsymbol{n} \, \mathrm{d}\varsigma$$

17

$$-\iint_{\Omega_\ell(t^n)} \widetilde{\lambda}_\ell(h^n)\widetilde{\vartheta}_\ell(h^n)\nabla h^{n+1} \cdot \nabla \left(\frac{\widetilde{\beta}_\ell(h^n)p_{test}}{p_0} \right) \mathrm{d}\boldsymbol{x} - \iint_{\Omega_g(t^n)} \widetilde{\lambda}_g(h^n)\widetilde{\vartheta}_g(h^n)\nabla h^{n+1} \cdot \nabla \left(\frac{\widetilde{\beta}_g(h^n)p_{test}}{p_0} \right) \mathrm{d}\boldsymbol{x}$$

where

$$\Omega_\ell(t) = \{\boldsymbol{x} \in \Omega_2 \,:\, h(t,\boldsymbol{x}) \leq h_\ell^s\} \quad and \quad \Omega_g(t) = \left\{\boldsymbol{x} \in \Omega_2 \,:\, h(t,\boldsymbol{x}) \geq h_g^s\right\}.$$

This would require to determine at each time iteration ❶ the location of the level sets $h(t^n,\cdot) = h_\ell^s$ and $h(t^n,\cdot) = h_g^s$ (possibly empty or not connected), ❷ to remesh so that the level sets coarsely coincide with the mesh edges, ❸ to increase the regularity of p_{test} and ❹ to fit the function $\frac{\partial \beta}{\partial h}$ involved in $\nabla \left(\widetilde{\beta}(h^n) \right) \approx \frac{\widetilde{\partial \beta}}{\partial h}(h^n)\nabla h^n$. Replacing the right hand side in (9a) *by the left hand side in* (9b) *enables to overcome all these issues.*

5 Numerical examples

Based on the numerical schemes detailed above, we perform some simulations aiming at:

1. validating our code by comparing to explicit steady solutions (dimension 1);

2. highlighting the better accuracy of the tabulated approach to describe the physics compared to the Stiffened Gas one (dimension 1 and 2);

3. showing the low influence of the thermal conduction for physically relevant data (dimension 2);

4. showing the ability of the model to capture the flow complexity by emphasising the influence of the gravity orientation (dimension 2).

Parameters are set as follows to simulate a PWR:

- Geometry:
  - 1D: $L_y = 4.2\,\mathrm{m}$
  - 2D: $L_x = 1\,\mathrm{m}$, $L_y = 2\,\mathrm{m}$

- Discretisation parameters:
  - 1D: $N = 100$ mesh nodes ($\Delta y \approx 4.2\,\mathrm{cm}$)
  - 2D: 40 nodes on the horizontal boundaries, 80 nodes on the vertical boundaries, which result in a mesh generated by FreeFem++ with 3740 vertices and a characteristic length of the mesh around $2\,\mathrm{cm}$
  - In both cases, the use of the method of characteristics make the numerical schemes unconditionally stable. Consequently, there is no constrain upon the time step. But to ensure a good accuracy, we cannot take a too large value for the time step. We set $\Delta t = 0.01\,\mathrm{s}$.

- Parameters involved in EOS:
  - Tabulated law: *cf.* § 2.3
  - Stiffened gas EOS: *cf.* [3, Table 1 in appendix]

- Reference values: $p_0 = 15.5\,\mathrm{MPa}$, $\Phi_0 = 170 \times 10^6\,\mathrm{W} \cdot \mathrm{m}^{-3}$, $\overline{v} = 0.5\,\mathrm{m} \cdot \mathrm{s}^{-1}$, $\mu_0 = 8.4 \times 10^{-5}\,\mathrm{kg} \cdot \mathrm{m}^{-1} \cdot \mathrm{s}^{-1}$

- Initial data:
  - 1D: $h_0(y) = h_e$, $v_0(y) = v_e + \int_0^y \beta(h_0(z))\Phi(0,z)/p_0\mathrm{d}z$ (well-prepared insofar as they satisfy the divergence constraint (9a))
  - 2D: $h_0(x,y) = h_e$, $\boldsymbol{u}_0(x,y) = (u_0(x,y), v_0(x,y)) = (0, 4\overline{v})$, $\Phi(x,y) = 20\Phi_0\mathbf{1}_{\{(x-0.5)^2+(y-0.5)^2 \leqslant 0.125^2\}}(x,y)$ (intense power density compactly supported in a disc in the lower part of the core)

5.1 1D simulations

We recall that this section is restricted to the case $\lambda = 0$.

In [3] we presented some analytical solutions for the 1D-LMNC model with phase change when the EOS is the Stiffened Gas law. This could not be achieved with tabulated values for the EOS. To assess our numerical scheme, we use steady solutions in the following proposition for any equation of state.

18

	y_ℓ^s	y_g^s
TAB	0.968	3.101
SG	0.964	4.001

Table 10: Location of appearance of mixture and vapour phases with the two approaches when the steady state is reached for the test of Section 5.1.1

Proposition 5.1. *We consider the steady case,* i.e. h_e, D_e *and* Φ *do not depend on time. Then, a steady solution to System* (9) *is*

$$h(y) = h_e + \frac{1}{D_e} \int_0^y \Phi(z)\, \mathrm{d}z,$$

$$v(y) = \frac{D_e}{\rho\big(h(y), p_0\big)} = \frac{D_e}{\rho\big(h_e, p_0\big)} + \int_y^L \frac{\beta\big(h(z), p_0\big)}{p_0} \Phi(z)\, \mathrm{d}z,$$

$$\overline{p}(y) = g \int_y^L \rho\big(h(z), p_0\big)\, \mathrm{d}z + D_e^2 \left(\frac{1}{\rho\big(h(L), p_0\big)} - \frac{1}{\rho\big(h(y), p_0\big)} \right) + \frac{\big[(2\mu + \eta)\beta\big]\big(h(y), p_0\big)}{p_0} \Phi(y).$$

Remark 5.1.

- *A distinctive feature of the* LMNC *model is that the steady enthalpy does not depend on the equation of state.*

- *Given the expression of h in Proposition 5.1, it can be stated whether the fluid appears only as a liquid phase (if $h(L_y) < h_\ell^s$) or as a mixture ($h_\ell^s \leq h(L_y) \leq h_g^s$) or as a vapour phase ($h(L_y) > h_g^s$).*

- *We do not state that this steady solution is an asymptotic solution as the latter's existence has not been proven yet for any EOS (except for the Stiffened Gas law and simple expressions for Φ [3]). But if there exists an asymptotic solution, it is necessary the one above.*

In the following 1D cases, we compare simulations obtained with the Stiffened Gas equation of state with the tabulated law. With the former EOS, we use Scheme `INTMOC_2` introduced in [3] while with the latter EOS, Scheme (14) (noted `MOC_2`) is involved.

5.1.1 Two-phase flow with phase transition

In the first test, we investigate the ability of our model to deal with two-phase flows with phase transition. The boundary conditions are $D_e(t) = 375\,\mathrm{kg} \cdot \mathrm{m}^{-2} \cdot \mathrm{s}^{-1}$, and $h_0(y) = h_e(t) = 1.190 \times 10^6\,\mathrm{J} \cdot \mathrm{K}^{-1}$. The power density is set constant in space and time and equal to Φ_0. With these parameters, the domain is initially filled with liquid.

Figure 8 displays numerical results for the enthalpy at instants $t = 2.8\,\mathrm{s}$ and $t = 4.0\,\mathrm{s}$, as well as velocity, temperature and Mach number fields at final time where the solution has already reached an asymptotic regime corresponding to Proposition 5.1.

We observe on Table 10 that mixture phases appear almost at the same location but the vapour phase appears quite earlier when using the tabulated values. These values (y_κ^s is such that $h(y_\kappa^s) = h_\kappa^s$) are computed from Proposition 5.1 and Table 7. They are recovered numerically. In this toy-case, it is worth emphasizing that our model predicts the appearance of some vapour at the top of the reactor due to a too small inflow velocity.

We also mention that the Mach number remains lower than 0.01 so that the low Mach number hypothesis is valid in this configuration.

5.1.2 A simplified scenario for a Loss of Flow Accident

Our model is then assessed on an accidental transient regime: a main coolant pump trip which is a Loss Of Flow Accident (LOFA). This set of data was already considered in [3] together with the Stiffened Gas law.

To simulate this scenario, the domain is initially filled with liquid water with a normal behaviour of the reactor: the pumps work normally and control rods are in upper position. The power density is equal to Φ_0 and we impose at the entrance the velocity $v_e = 10\overline{v}$. These constants are chosen so as to prevent the appearance of mixture. The asymptotic state is reached at $t \simeq 0.8\,\mathrm{s}$ with SG and $t \simeq 0.9\,\mathrm{s}$ with TAB.

At time $t_1 = 1.5\,\mathrm{s}$ most of the pumps stop, so that the entrance velocity decreases. At time t_2, the security system detects the presence of mixture and makes control rods drop into the core decreasing abruptly the power density. However, there is still some residual power density (about $7\%\Phi_0$). We measured $t_2 \simeq 2.85\,\mathrm{s}$ with SG and $t_2 \simeq 2.57\,\mathrm{s}$
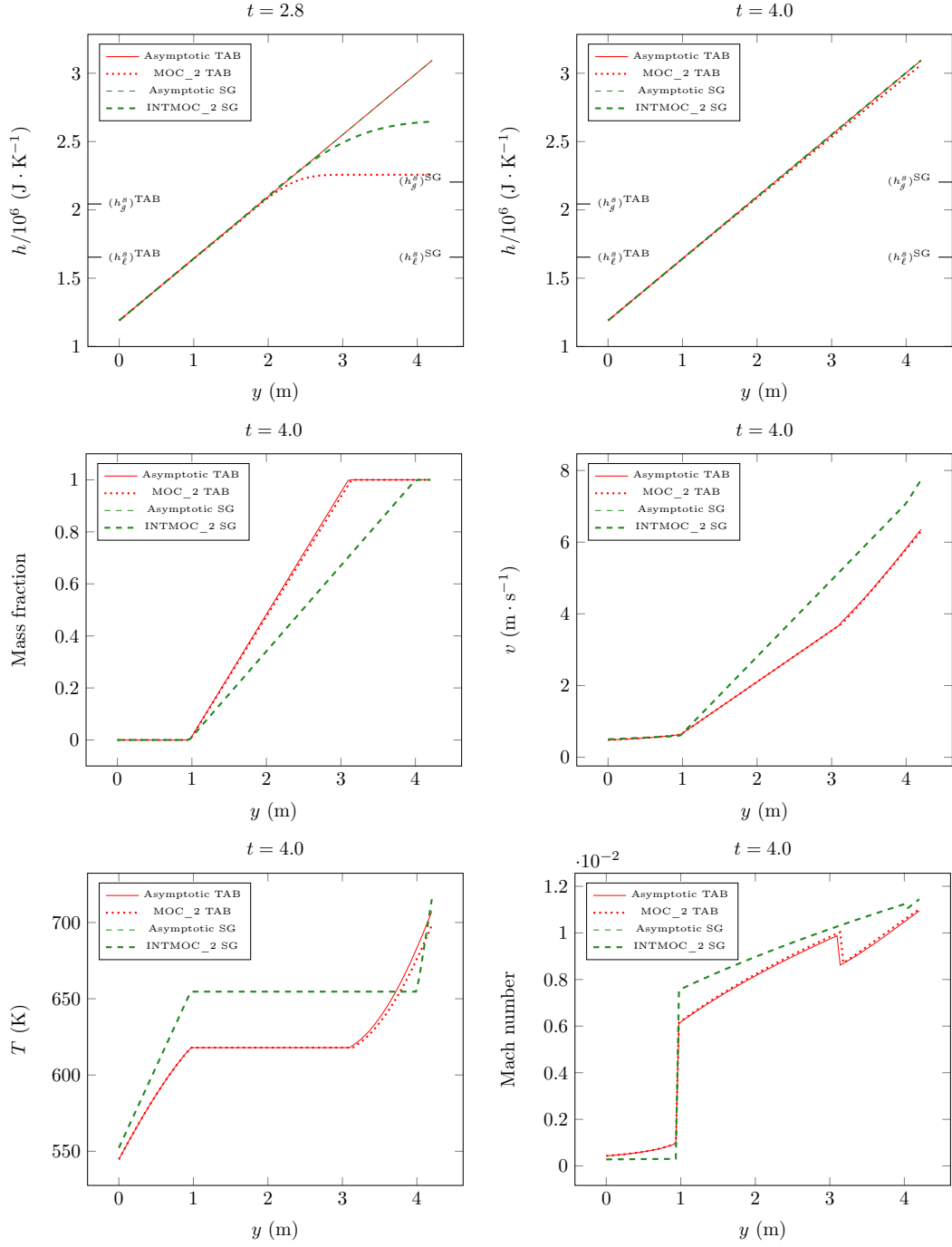
Figure 8: Comparisons of numerical schemes: transient and asymptotic enthalpy, asymptotic mass fraction, velocity, temperature and Mach number for the test of Section 5.1.1

with TAB. At time $t_3 = 20\,\text{s}$ the security pumps are turned on, thus the inflow is re-established. We then compute the solution until the asymptotic state is reached.

Functions $v_e(t)$ and $\Phi(t)$ can be modelled as follows (see Figure **??**):

$$v_e(t) = \begin{cases} 10\overline{v} & \text{if } 0 \leq t < t_1, \\ 0.2\overline{v} & \text{if } t_1 \leq t < t_3, \\ 10\overline{v} & \text{if } t \geq t_3, \end{cases} \qquad\qquad \Phi(t) = \begin{cases} \Phi_0 & \text{if } 0 \leq t < t_2, \\ 7\%\Phi_0 & \text{if } t \geq t_2. \end{cases}$$

On Figures 9 we report the behaviour of the mass fraction and temperature computed at different instants for both EOS. Since we chose $t_3 = 20\,\text{s}$, the pumps are re-started soon enough so that the core is not entirely vaporised. We notice that the stiffened gas EOS provides underestimated values for the mass fraction which is detrimental for safety evaluations.

5.2 2D simulations

The following numerical results deal with dimension 2 and focus on the incorporation of the tabulated EOS in the FREEFEM++-code based on Section 4.2 and previously applied to the monophasic nondiffusive case with Stiffened Gas law in [9]. We are interested in the influence of the thermal conductivity and of the gravity field upon the flow. We finally carry out a comparison with some results obtained with the Stiffened Gas law. The setting is as follows: the power density is here compactly supported within a disc in the lower part of the core, which yields a genuine 2D case.

5.2.1 Influence of the thermal conductivity

The temperature increases as the flow passes through the heat source and some mixture appears. The mixture phase has a lower density than the liquid phase. Hence, as the flows goes upwards and the gravity field is pointing downwards, a Rayleigh-Taylor instability occurs (see Figure 10(c)): the gravity makes the lighter phase speed up through the heavier phase above. The instability is well recovered by the numerical scheme over this mesh.

The thermal conductivity is of order 1 in this case. We observe on Figure 10(f) the difference between numerical solutions with and without thermal diffusion at time $0.40\,\text{s}$. The error is of order 10^{-4}, which shows that for the physical situations we are interested in, the thermal conductivity does not play a major role.

5.2.2 Influence of the gravity field

As the previous computations showed the low influence of the thermal conductivity in these experiments, we set $\lambda \equiv 0$ in the sequel. Since our choice of power density generates hydrodynamic instabilities apparently driven by gravity effects, we focus on the impact of the gravity field direction.

Figures 11 depict the same test case than previously except for the gravity field whose orientation varies (downwards/null/upwards/to the right).

In the classical situation where the gravity is oriented downwards (Figure 11(a)), the flow driven by the material velocity is sped up by the gravity effects which makes the mixture phase go upwards. Without gravity (Figure 11(b)), there is a unique physical phenomenon (forced convection) that governs the motion of fluid which explains that at the same time of evolution, the mixture cloud is lower than in the previous case (but hotter as the fluid remained longer within the core) and no Rayleigh-Taylor instability occurs. If the gravity field is upward (Figure 11(c)), there is a balance between the two aforementioned phenomena. The flow velocity makes the mixture go to the top while the gravity makes it go to the bottom as it is lighter compared to the pure liquid phase. The motion is even slower than without gravity. As for the horizontal case (Figure 11(c)), the y-velocity is equivalent to the downward case but we observe that the mixture tends to the left which is the opposite direction to the gravity field as expected. Hence, we see that our numerical scheme enables to catch various types of behaviour depending on the data.

5.2.3 Influence of the EOS

The 2D test cases proposed in Section 5.2.1 and 5.2.2 were run with the tabulated approach based on the NIST tables according to the procedure detailed in Section 2.3. We finally provide some results highlighting the influence of the EOS in this specific 2D case (without thermal conduction).

We consider the same framework as in the previous 2D cases but the equation of state differs: either the tabulated law (same results as above) – denoted by TAB –, or the Stiffened Gas law as in [3] – denoted by SG. Figures 12 depict the L^2-norm of h, $\boldsymbol{u}$ and α. Let us first give some comments about the evolution of the process. At time $t_1 \approx 0.10\,\text{s}$, we observe a distinction between the two simulations. It is the time at which the mixture phase appears. Then the change of monotonicity (at times $t_2^{\text{SG}} \gtrsim 0.5\,\text{s}$ for the Stiffened Gas law vs. $t_2^{\text{TAB}} \lesssim 0.6\,\text{s}$ with tabulated values) of all variables corresponds to the time at which the Rayleigh-Taylor instability reaches the top of the core and exits.

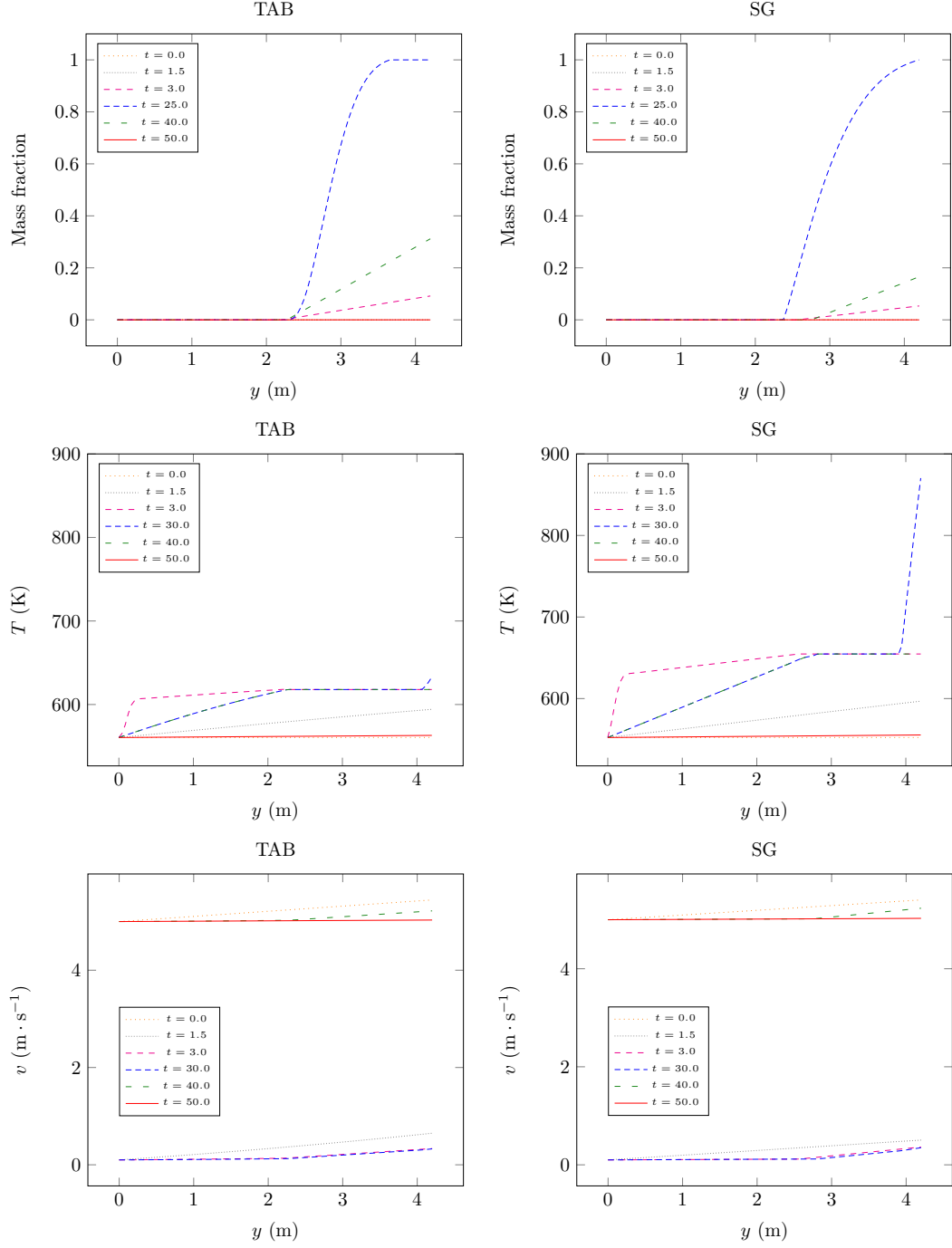Figure 9: Numerical temperature with Tabulated EOS (left) and Stiffened Gas EOS (right) of the test of Section 5.1.2
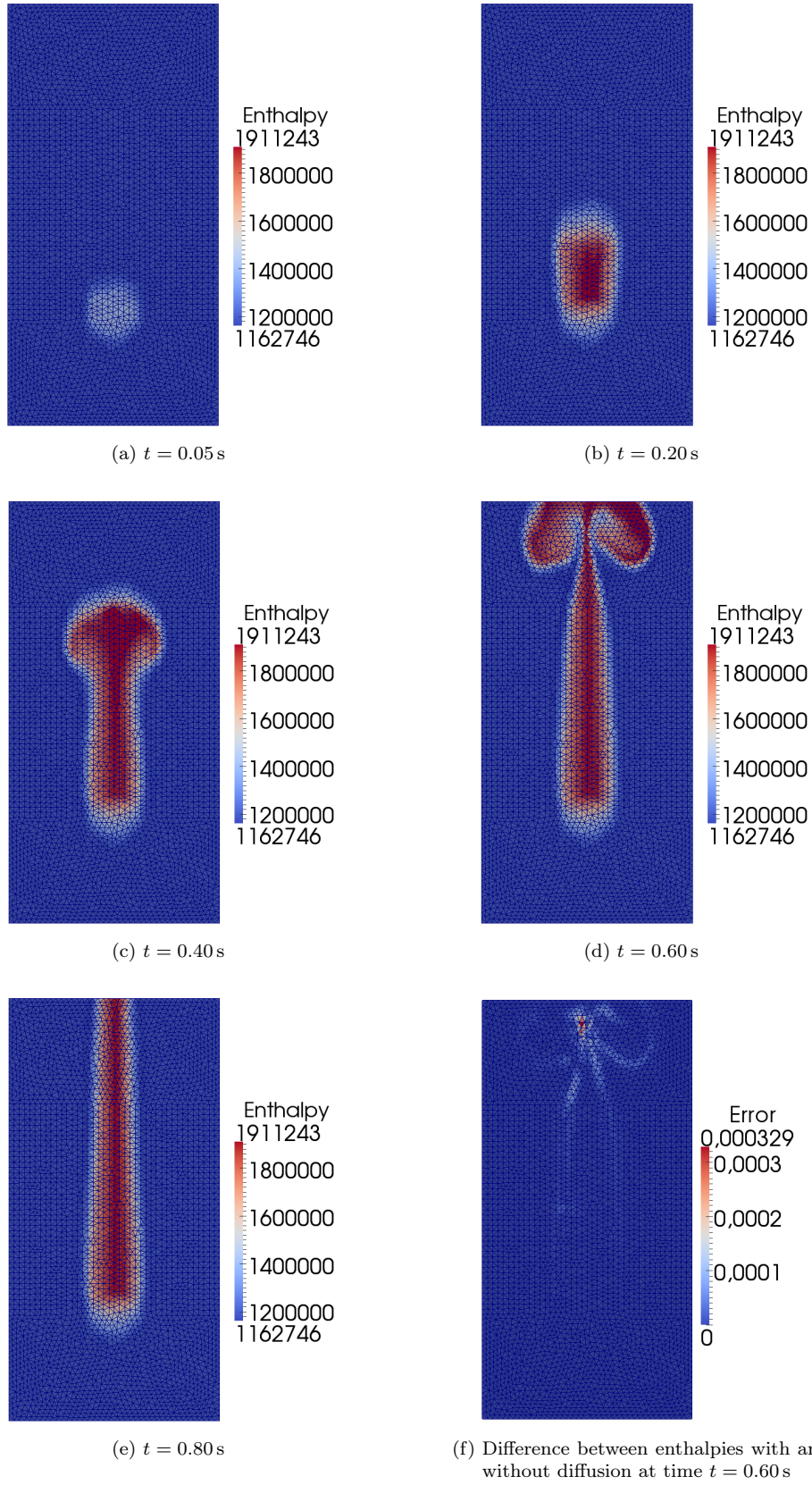
(a) $t = 0.05\,\text{s}$

(b) $t = 0.20\,\text{s}$

(c) $t = 0.40\,\text{s}$

(d) $t = 0.60\,\text{s}$

(e) $t = 0.80\,\text{s}$

(f) Difference between enthalpies with and without diffusion at time $t = 0.60\,\text{s}$

Figure 10: Enthalpy for a flow with thermal diffusion and comparison with the non-diffusive case for the test of Section 5.2.1
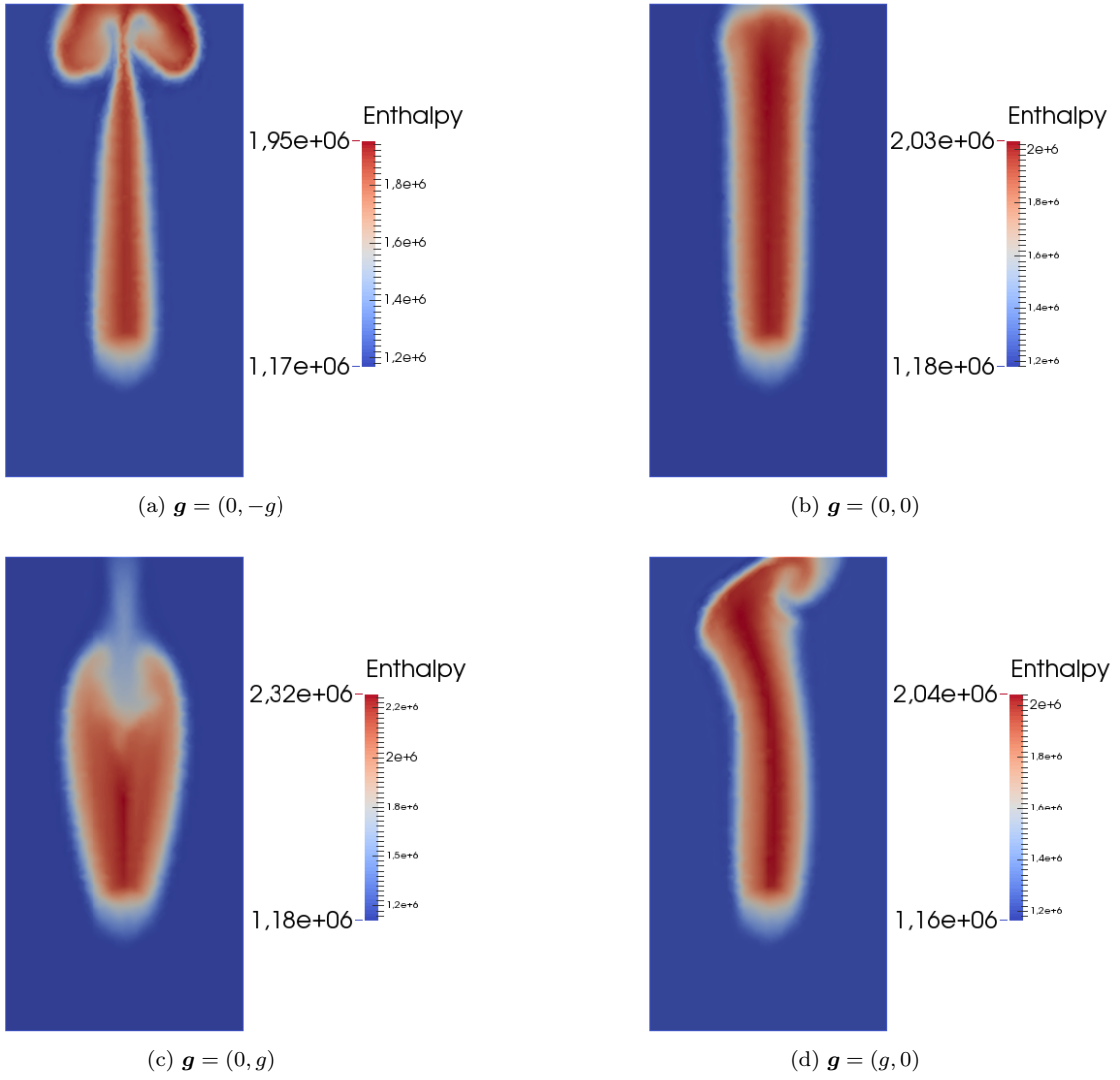
(a) $\boldsymbol{g} = (0, -g)$

(b) $\boldsymbol{g} = (0, 0)$

(c) $\boldsymbol{g} = (0, g)$

(d) $\boldsymbol{g} = (g, 0)$

Figure 11: Influence of the gravity field at time $0.60\,\mathrm{s}$ for the test of Section 5.2.2

More precisely, although the two simulations (Figures 13) yield coarsely the same shape for the flow, we notice that the results are quantitatively different: we observed that the Stiffened Gas EOS overestimates the compressibility coefficient in the mixture (*cf.* Fig. 4(c)) which implies larger values for the velocity field between t_1 and t_2 (see Figure 12(b)). As a result, the instability reaches the top of the core faster with SG than with TAB.

The fluid being convected faster in the SG case, it thus spends less time than in the TAB case and one may expect that the enthalpy might be smaller, which is not in accordance with Figure 12(a). This may be explained by the fact that the density is underestimated by the Stiffened Gas law (*cf.* Fig. 4(a)). Hence the source term in the transport equation for h, $\Phi/\varrho(h, p_0)$ is overestimated and the enthalpy is larger in the SG case.

Let us note that monotonicities of h and α on Figures 12(a) and 12(c) are coherent with each other due to the fact that, differentiating (2) for $\alpha \in \,]0, 1[$, we have

$$\frac{\partial \alpha}{\partial h}(h, p_0) = \frac{[\rho_\ell^s \rho_g^s (h_g^s - h_\ell^s)](p_0)}{\left\{ \left[\rho_g^s h_g^s - \rho_\ell^s h_\ell^s \right](p_0) - h \cdot \left[\rho_g^s - \rho_\ell^s \right](p_0) \right\}^2} > 0,$$

since $h_g^s > h_\ell^s$ for both SG and TAB EOS.

As for the 1D test cases of Section 5.1, the latter results underline that the equation of state may play a major role in the modelling of heat exchanges in nuclear reactor cores, which legitimates the present approach based on the NIST tables rather than the use of the Stiffened Gas law as in previous papers.

Acknowledgements: NEEDS

## 6 Conclusion & Perspectives

The process of modelling physical phenomena requires to improve models and algorithms step by step. While we assessed the LMNC model and 1D/2D numerical strategies in previous publications, we introduced in this paper the approach of tabulated equations of state to obtain a better accuracy in the range of high temperatures. From a theoretical point of view, it comes down to replace the analytical Stiffened Gas law by fitting polynomials for each thermodynamic variable. A drawback is the impossibility to derive explicit unsteady solutions even in dimension 1 but it is still possible to obtain a steady state. From a numerical point of view, this approach does not raise particular issues. It turns out to provide much more relevant results from the physical point of view whether it be in dimensions 1 or 2. The Stiffened Gas law is shown to be irrelevant in the range of temperatures at stake but it enabled in previous works to better understand the structure of the model and to develop robust 1D and 2D numerical schemes now adapted to the new strategy (tabulated law).

A first study about the influence of the thermal conductivity was also carried out in this paper. Further investigations will be led in future works especially in dimension 1 where the appearance of pure vapour raises several issues when thermal conductivity is taken into account.

The fact that in this modelling the thermodynamic pressure is constant, is a major advantage for the TAB-LMNC model as the fitting polynomials are computed primary to the overall resolution of the PDEs. Indeed, for a standard compressible model, fitting polynomials would be different at each time step and each space node, due to the dependance on the thermodynamic pressure, which is not constant anymore. Hence there is no extra computational time induced by the tabulated EOS. To continue enriching the modelling, time-varying pressures will be considered to account for depressurisation processes (see [4] for Stiffened Gas law). As well, simulations in dimension 3 which are much more time-consuming will also be contemplated.
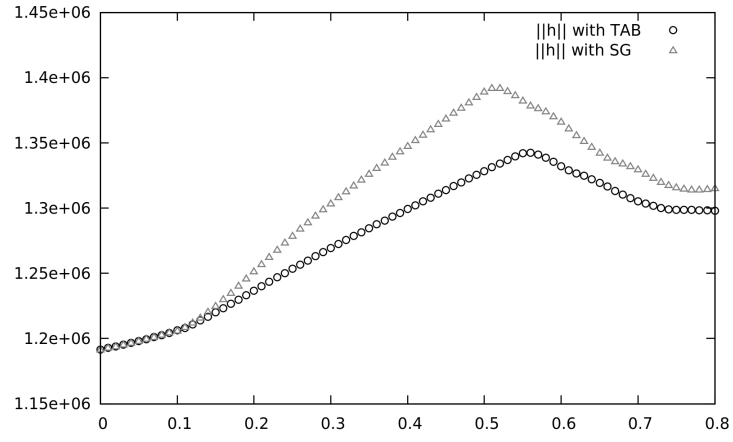
(a) $\|h(t, \cdot)\|_{L^2}$
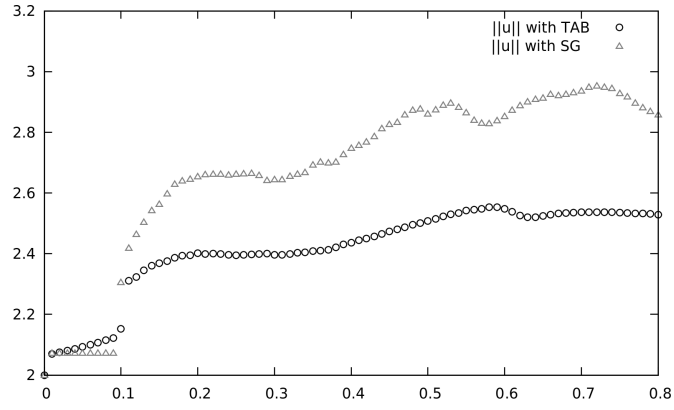
(b) $\|\boldsymbol{u}(t, \cdot)\|_{L^2}$
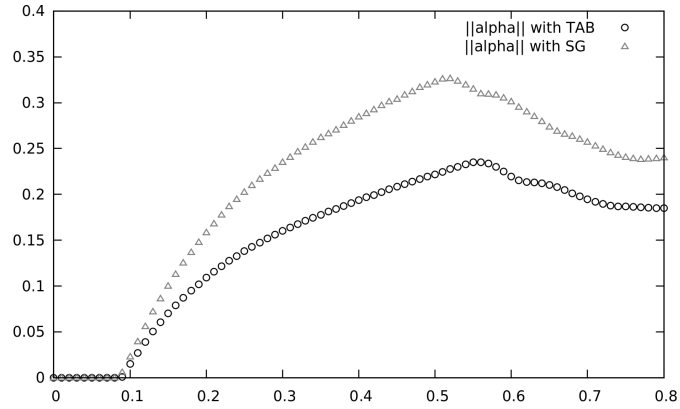
(c) $\|\alpha(t, \cdot)\|_{L^2}$

Figure 12: Influence of the EOS: L^2-norm of enthalpy, velocity and volume fraction fields for $t \in [0, 0.8]$ for the test of Section 5.2.3
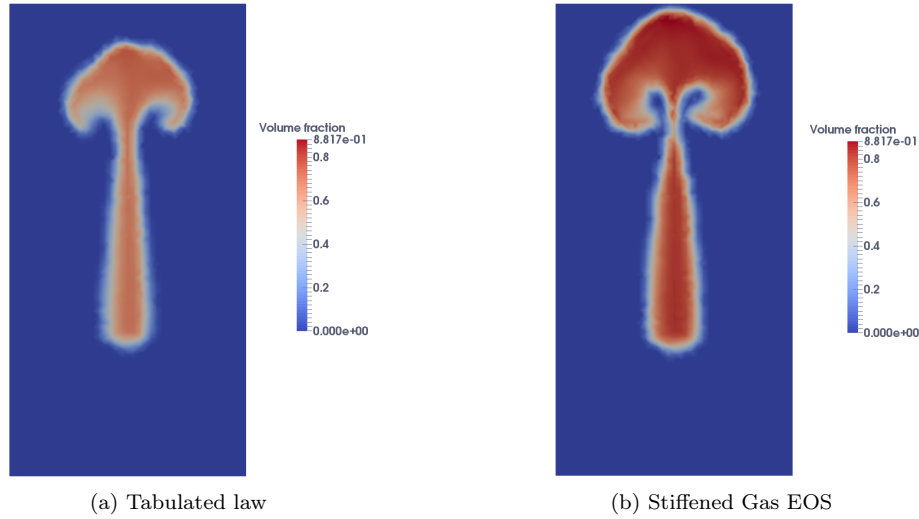
(a) Tabulated law   (b) Stiffened Gas EOS

Figure 13: Influence of the EOS: volume fraction α at time $0.50\,\mathrm{s}$ for the test of Section 5.2.3

References

[1] G. Allaire, G. Faccanoni, and S. Kokh. A strictly hyperbolic equilibrium phase transition model. *C. R. Acad. Sci. Paris Sér. I*, 344:135–140, 2007.

[2] M. Bernard, S. Dellacherie, G. Faccanoni, B. Grec, O. Lafitte, T.-T. Nguyen, and Y. Penel. Study of low Mach nuclear core model for single-phase flow. In *ESAIM:Proc*, volume 38, pages 118–134, 2012.

[3] M. Bernard, S. Dellacherie, G. Faccanoni, B. Grec, and Y. Penel. Study of a low Mach nuclear core model for two-phase flows with phase transition I: stiffened gas law. *Math. Model. Numer. Anal.*, 48(6):1639–1679, 2014.

[4] A. Bondesan, S. Dellacherie, H. Hivert, J. Jung, V. Lleras, C. Mietka, and Y. Penel. Study of a depressurisation process at low Mach number in a nuclear core reactor. 2016.

[5] H. B. Callen. *Thermodynamics and an Introduction to Thermostatistics*. John Wiley & sons, second edition, 1985.

[6] S. Clerc. Numerical Simulation of the Homogeneous Equilibrium Model for Two-Phase Flows. *J. Comput. Phys.*, 181(2):577–616, 2002.

[7] J.M. Delhaye. *Thermohydraulique des réacteurs*. EDP sciences, 2008.

[8] S. Dellacherie. On a low Mach nuclear core model. In *ESAIM:Proc*, volume 35, pages 79–106, 2012.

[9] S. Dellacherie, G. Faccanoni, B. Grec, E. Nayir, and Y. Penel. 2D numerical simulation of a low Mach nuclear core model with stiffened gas using FreeFem++. In *ESAIM:ProcS*, volume 45, pages 138–147, 2014.

[10] G.A. Dilts. Consistent thermodynamic derivative estimates for tabular equations of state. *Phys. Rev. E*, 73(6):066704, 2006.

[11] G. Faccanoni. *Étude d'un modèle fin de changement de phase liquide-vapeur. Contribution à l'étude de la crise d'ébullition*. PhD thesis, École Polytechnique, France, November 2008.

[12] G. Faccanoni, S. Kokh, and G. Allaire. Approximation of liquid-vapor phase transition for compressible fluids with tabulated EOS. *C. R. Acad. Sci. Paris Sér. I*, 348(7):473–478, 2010.

[13] G. Faccanoni, S. Kokh, and G. Allaire. Modelling and simulation of liquid-vapor phase transition in compressible flows based on thermodynamical equilibrium. *Math. Model. Numer. Anal.*, 46:1029–1054, 2012.

[14] W. Greiner, L. Neise, and H. Stöcker. *Thermodynamics and statistical mechanics*. Springer, 1997.

[15] F.H. Harlow and A.A. Amsden. Fluid dynamics-an introductory test. Technical Report LA 4100, Los Alamos National Lab., 1970.

[16] F. Hecht. New development in FreeFem++. *J. Numer. Math.*, 20(3-4):251–266, 2012.

[17] P. Helluy and H. Mathis. Pressure laws and fast legendre transform. *Math. Models Methods Appl. Sci.*, 21(04):745–775, 2011.

[18] O. Le Métayer, J. Massoni, and R. Saurel. Elaborating equations of state of a liquid and its vapor for two-phase flow models. *Int. J. Therm. Sci.*, 43(3):265–276, 2004.

[19] E.W. Lemmon, M.O. McLinden, and D.G. Friend. *Thermophysical Properties of Fluid Systems*. National Institute of Standards and Technology, Gaithersburg MD, 20899.

[20] R. Menikoff and B.J. Plohr. The Riemann problem for fluid flow of real materials. *Rev. Mod. Phys.*, 61(1):75–130, 1989.

[21] A. Morin and T. Flåtten. A two-fluid four-equation model with instantaneous thermodynamical equilibrium. *Math. Model. Numer. Anal.*, 2015.

[22] S. Müller and A. Voss. The Riemann problem for the Euler equations with nonconvex and nonsmooth equation of state: construction of wave curves. *SIAM J. Sci. Comput.*, 28(2):651–681 (electronic), 2006.

[23] S.L. Passman, J.W. Nunziato, and E.K. Walsh. A theory of multiphase mixtures. In *Rational Thermodynamics*, pages 286–325. Springer New York, 1984.

[24] Y. Penel. An explicit stable numerical scheme for the 1d transport equation. *Discrete Contin. Dyn. Syst. Ser. S*, 5(3):641–656, 2012.

[25] R. Saurel, F. Petitpas, and R. Abgrall. Modelling phase transition in metastable liquids: application to cavitating and flashing flows. *J. Fluid Mech.*, 607:313–350, 2008.

[26] N.E. Todreas and M.S. Kazimi. *Nuclear Systems I: Thermal Hydraulic Fundamentals*, volume 2. Taylor & Francis, 1990.

[27] A. Voss. *Exact Riemann solution for the Euler equations with nonconvex and nonsmooth equation of state*. PhD thesis, RWTH Aachen, 2005.